Built-in Self-Test for RF Impedance Measurement

by

Muslum Emir Avci

A Dissertation Presented in Partial Fulfillment
of the Requirements for the Degree
Doctor of Philosophy

Approved November 2023 by the
Graduate Supervisory Committee:

Sule Ozev, Chair
Jennifer Kitchen
Bertan Bakkaloglu
George Trichopoulos

ARIZONA STATE UNIVERSITY

December 2023

ABSTRACT

Impedance is one of the fundamental properties of electrical components, materials, and waves. Therefore, impedance measurement and monitoring have a wide range of applications. The multi-port technique is a natural candidate for impedance measurement and monitoring due to its low overhead and ease of implementation for Built-in Self-Test (BIST) applications. The multi-port technique can measure complex reflection coefficients, thus impedance, by using scalar measurements provided by the power detectors. These power detectors are strategically placed on different points (ports) of a passive network to produce unique solution.

Impedance measurement and monitoring is readily deployed on mobile phone radio-frequency (RF) front ends, and are combined with antenna tuners to boost the signal reception capabilities of phones. These sensors also can be used in self-healing circuits to improve their yield and performance under process, voltage, and temperature variations. Even though, this work is preliminary interested in low-overhead impedance measurement for RF circuit applications, the proposed methods can be used in a wide variety of metrology applications where impedance measurements are already used. Some examples of these applications include determining material properties, plasma generation, and moisture detection. Additionally, multi-port applications extend beyond the impedance measurement. There are applications where multi-ports are used as receivers for communication systems, RADARs, and remote sensing applications.

The multi-port technique generally requires a careful design of the testing structure to produce a unique solution from power detector measurements. It also requires the use of nonlinear solvers during calibration, and depending on calibration procedure, measurement. The use of nonlinear solvers generates issues for convergence, computational complexity, and resources needed for carrying out calibrations and

measurements in a timely manner.

In this work, using periodic structures, a structure where a circuit block repeats itself, for multi-port measurements is proposed. The periodic structures introduce a new constraint that simplifies the multi-port theory and leads to an explicit calibration and measurement procedure. Unlike the existing calibration procedures which require at least five loads and various constraints on the load for explicit solution, the proposed method can use three loads for calibration. Multi-ports built with periodic structures will always produce a unique measurement result. This leads to increased bandwidth of operation and simplifies design procedure. The efficacy of the method demonstrated in two embodiments. In the first embodiment, a multi-port is directly embedded into a matching network to measure impedance of the load. In the second embodiment, periodic structures are used to compare two loads without requiring any calibration.

DEDICATION

My family, and friends

ACKNOWLEDGMENTS

I would like to extend my deepest gratitude to my advisor Dr. Sule Ozev for her guidance and patience during my PhD studies. Her kindness and support made the challenges during the PhD process much easier to overcome. She also provided support in terms of funding, technical advice, and equipment. I will be forever grateful for her support.

I would also like to extend my sincere thanks to Dr. Jennifer Kitchen for her support, and letting me use her measurement equipment that enabled all the experiments in this dissertation. Without her support this dissertation just would be theory and simulation.

I also would like to express my appreciation for my committee members, Dr. Kitchen, Dr. Bertan Bakkaloglu and Dr. Georgios Trichopoulos, who took their valuable time to be in my committee.

I also would like to thank my friends, who provided conversations, jokes and support during challenging times. Finally, I would like to my gratitude to my parents, and sister for their support for all my pursuits, and dreams. Without my friends and family, I would not be able to overcome spiritual and psychological challenges inherent to the research process and life.

TABLE OF CONTENTS

Page

CHAPTER Page

LIST OF TABLES

LIST OF FIGURES

Figure Page

Figure Page

Chapter 1

INTRODUCTION

Increasing performance demands of the next generation wireless technologies necessitates post-production and in-field tuning of RF components to achieve the design goals in terms of efficiency, linearity, and noise. The performance metrics are affected by the process, voltage, and temperature (PVT) variations and environmental conditions. RF systems are also used in applications where functional safety has utmost importance, such as automotive mmWave RADARs, requiring in-field testing during the deployment period. Meeting performance demands in these adverse conditions becomes even more challenging for multiple-input multiple-output (MIMO) devices, which uses multiple amplifiers to achieve its functionality. In a MIMO application, each input and output device should be tested to ensure system can achieve its full capability.

To ensure the RF system meets system requirements, extensive simulations are used to determine performance bounds and include calibration knobs when necessary at the design phase [1–3]. To compensate for degraded performance due to these variations, generally an adaptive element or a network is incorporated between the source and the load, which enables post-production calibration. This adaptive element can be realized by many methods but the most common methods are: using switched capacitor or inductor banks, electronically adjustable capacitors (varactor), adjusting the biasing current of the amplifiers. The different controls over the system provided by these adaptive elements are referred as the tuning knobs of the system. Each adaptive element provides us a degree-of-freedom to adapt and improve the performance of the system in different conditions. In post-production testing and calibration, circuit

parameters are adjusted using these included tuning knobs to minimize the effects of PVT variations in circuit performance and achieve the desired performance [4–6]. The dynamic environmental changes, such as temperature, aging, objects in near-field of the antenna cannot be accounted in post-production testing [7–11]. Therefore, these changes necessitate in-field testing. Additionally, both in post-production test and in-field test, measurement with external devices may not be feasible due to physical limitations, such as measuring power or impedance in an internal node of an integrated circuit. In these cases using an external equipment for the measurement would generate a difference between the two nodes and the measurement plane. Furthermore, external equipment cannot be used for in-field measurements. To overcome these challenges, Built-in Self Test (BIST) techniques can be used for measurement. Different BIST sensors can be deployed in different points of the system, and the circuit, including the internal nodes that are not available for external measurements. These measurements then can be used to infer overall performance of the system, and do the necessary adjustments to the tuning knobs to maximize the performance of the system while being deployed, enabling in-field testing. BIST techniques also shift the burden from using external RF equipment to internal monitoring during post-production testing and calibration reducing the testing cost and time [12–20].

One tuning metric, that effects virtually all performance metrics in RF circuits is the impedance and relative relations of the impedances in various nodes in the circuit, such as the matching between the receiver amplifier and the receiver antenna. The matching between the antenna and the amplifier is critical in order to meet system-level requirements [21]. On top of the PVT variations, the matching can shift due to environmental conditions. The input impedance of the antenna changes depending on objects and materials in the near-field, the antenna array configuration, the mutual coupling between antennas, and the scan angle of the antennas [21,22]. The variation

in input impedance of the antenna in turn effects the performance of the transmitters and receivers. The matching between an amplifier and its load controls the overall gain of the system, the noise figure, the efficiency and the linearity [23,24]. From these examples, it can be surmised that one of the critical parameters for proper operation of these elements is the impedances of the amplifier and antenna, which can be quantified by the reflection coefficient (S_{11}, Γ) between a source and a load. Therefore, in-field monitoring of the impedance of different nodes in the circuit, without disrupting the circuit operation, is necessary.

Impedance measurement and monitoring is readily deployed on mobile phone RF front ends, and they are combined with antenna tuners to boost the signal reception capabilities of the phones [25, 26]. These sensors also can be used in self-healing circuits to improve their yield and performance under process, voltage, and temperature variations [27]. The multi-port technique is a natural candidate for impedance measurement and monitoring due to its low overhead and ease of implementation for Built-in Self-Test (BIST) applications [28, 29]. The multi-port technique can measure complex reflection coefficients (Γ), thus impedance, by just using scalar measurements provided by the power detectors. It is one of the few ways to measure complex impedance without using a tuned receiver. This technique generally requires a careful design of the testing structure to produce a unique solution from power detector measurements. It also requires the use of nonlinear solvers during calibration, and depending on the calibration procedure, the measurement phase. This also generates additional issues for convergence, computational complexity, and resources needed for carrying out calibrations and measurements in a timely manner. Various implementations of multi-port reflectometer systems shown to be appropriate for the integrated circuit applications [30–32].

1.1 Impedance Measurement Techniques in RF Frequencies

There are many different approaches that are developed to measure impedance in RF frequencies in the current literature, with different trade-offs, requirements and components. The most direct approach for measuring S_{11} or RF impedance is using a directional coupler to separate incident and reflected waves. This approach is generally used by vector network analyzers (VNAs). A traditional VNA is built by using directional coupler, and two full path receivers to measure the magnitude and phase of incident and reflected waves. Then amplitude and phase information is used to measure S_{11}. Unfortunately, each receiver needs its own mixer, filters, and amplifiers to accurately measure impedance. Therefore, this approach is prohibitive for embedded applications and in-field testing due to its high overhead, both in terms of required area, and power consumption. Instead of full-path receivers, low-overhead sensors such as power detectors can be used to measure impedance. There are different approaches to utilize power detectors to measure S_{11} or impedance directly. In [33–35], directional couplers are used with power detectors to calculate the magnitude of the S_{11}. In addition to directional couplers, a circulator also can be used to separate incident and reflected waves as demonstrated in [36]. These methods are similar to VNA, but they only measure the amplitude of the S_{11}. Because by themselves, power detectors provide only scalar measurements and do not give information about the phase. This challenge can be overcome by using multiple power detectors. The power of different linear combinations of incident and reflected waves can be measured to extract information about their relative phases. To achieve this, generally combiners and phase shifters are used in addition to directional couplers, then the magnitude of the linear combinations are measured by the power detectors to find the relative phase information. The six-port/multi-port theory generalizes this

notion and provides a mathematical framework for calculating magnitude and phase of S_{11} or impedance using linear networks and power detectors [37]. A multi-port network analyzer consists of a passive network with at least six ports. Four ports are used for the power detectors, and the other two ports are used for the signal source and device under test (DUT) as shown in Fig. 1.1. The multi-port theory describes the relation between impedance of DUT, the linear network parameters that are determined at the design time and the power detector measurements. In multi-port network analyzers, couplers, phase shifters, and combiners are carefully designed and power detectors are strategically placed in various points of the circuit to maximize measurement sensitivity and accuracy, while minimizing the required dynamic range. There are a wide range of multi-port network analyzer design options ranging from integrated [30–32, 38], to board level [39, 39–41] implementations.

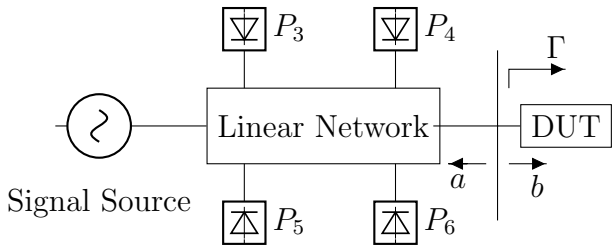

Figure 1.1: Basic Multi-Port Network Analyzer for Measuring Γ

1.2 Six-Port Network Analyzers

The most common implementation of such network analyzers is referred to as the six-port reflectometer (SPR). Reflectometers typically have one test port to measure the reflection coefficient, (Γ, S_{11}), as shown in Fig. 1.1. Two of the six-ports are used as RF input and DUT ports and the remaining four ports are terminated with power detectors and serve as measurement ports. These four power measurements provide four equations to solve for Γ. In addition to the SPR, reflectometers with five or more

than six ports have also been proposed [42–44]. By extension, two or more SPRs can be combined to create a two-port network analyzer [44, 45].

In order to minimize the number of components in a reflectometer, the multi-state reflectometer architecture is proposed in [46]. This type of reflectometer is a trade-off between number of components and the test time. There are only two power detectors required for this structure, but measurements must be taken in several steps. For example, to mimic the SPR, a multi-state reflectometer needs four steps to complete the measurements. In each step, the network parameters need to be changed such that, it is equal to its SPR counterpart.

The most widely used model for SPR (and its multi-state equivalent) is developed in [37]. In this model, it is assumed that power detectors are connected to the DUT by a linear network. Therefore, the power incident upon each detector, (P_n), is related to Γ with the following equation:

$$P_n = |A_n a + B_n b|^2 \tag{1.1}$$

where A_n, B_n are network parameters. This equation can be rearranged into the following form:

$$P_n = |A_n|^2 |b|^2 |\Gamma - q_n|^2 \tag{1.2}$$

where $q_n = -B_n/A_n$ and $\Gamma = a/b$. In this architecture, a reference port, P_0, is chosen, such that P_0 is predominantly a function of the incident power to DUT ($A_0 \approx 0$). By taking the ratio of power incident upon each port, P_n, to the power incident upon a reference port, P_0, measurements can be decoupled from the incident power. Since $A_0 \approx 0$, P_0 is expressed as, $P_0 = |B_0|^2 |b|^2 |1 + A_0/B_0\Gamma|^2$. Thus, the power ratio, P_n/P_0 is expressed in the following form:

$$|\Gamma - q_n|^2 = \left|\frac{B_0}{A_n}\right|^2 \cdot \frac{P_n}{P_0} \tag{1.3}$$

In [37], each such ratio is treated as a circle, with the center at q_n, and the radius $|B_0/A_n|^2 \cdot P_n/P_0$. Intersection point of these circles in the complex plane yields the Γ. Therefore, the performance of the SPR is dependent on the selection of q_n parameters. In [37], the author concludes that a 120° separation between these parameters to be optimal due to the presumed symmetry of the architecture $|q_4|= |q_5|= |q_6|$. These proposed parameters are widely used in current literature. However, this process, based on geometric intuition does not take non-idealities in hardware components into account and it does not provide an insight for alternative designs where power ratios may not be interpreted as circles.

1.3 Contributions

The contributions of this work to multi-port design and use can be summarized as:

- A theoretical framework for minimizing impact of noise to the measurements.
- Overcoming the computational complexity by eliminating the use of nonlinear solvers in calibration and measurement.
- Simplifying the calibration procedure by reducing the number of required calibration loads.
- In certain applications eliminating the calibration procedure all together.

1.4 Thesis Organization

This thesis organized into five chapters. In this chapter (Chapter 1), motivation and brief background information on multi-port technique is given. In Chapter 2, literature review of the multi-port techniques is given. A theoretical framework for

minimizing impact of noise to multi-port measurement is given in Chapter 3. The proposed theory is verified with simulations and the derived design parameters are used to realize a multi-state reflectometer. In Chapter 4, using periodic structures as multi-ports is proposed. In this chapter, in depth analysis of periodic structures as multi-port is given and a calibration technique is proposed. The use of periodic structures as multi-ports and the analysis is verified with simulations and hardware experiments. A technique that uses periodic structures for comparing two impedance values in relation to each other is given in Chapter 5. This technique is verified with simulation and hardware experiments. All chapters except the Chapter 1 and 2, have the following structure: theory, simulation verification, hardware experiment verification.

Chapter 2

LITERATURE REVIEW

Multi-port calibration methods in the current literature make different trade-offs between calibration complexity, measurement complexity, the number of constraints, and the number of known loads. Nonlinear solvers can be used for both calibration and measurement phases to directly solve for network parameters with four known loads [47]. By using more than four known loads, this direct approach can be used for calibrating nonidealities in the system, such as power detector nonlinearities [48]. In the cases where these nonidealities are not significant, nonlinear solvers are still necessary to solve for expressions involving exponentiation and multiplication of underlying network parameters. These expressions can be treated as additional unknowns to simplify calibration and measurement procedures at the expense of using more calibration loads. In [49–51], five known loads are used to produce an explicit calibration and measurement procedure. The number of known quantities is relaxed in [52, 53] where calibration reflection coefficients do not need to be known but their magnitudes should be equal. Another calibration approach is proposed in [54], which requires a known load in addition to several unknown loads which cover the desired measurement region in the Smith Chart. However, in [52–54] a nonlinear solver (or an optimizer) is required for calibration. The physical model of the transmission line and the assumption of high impedance power probes are used to simplify underlying multi-port relations and derive explicit measurement and calibration procedures in [42]. A comparison of the calibration methods is given in Table-2.1.

In multi-port reflectometers, two ports are used as RF input and DUT ports and the remaining ports are used as measurement ports, which are generally ter-

minated with power detectors. The number of ports can be adjusted to improve the accuracy and the bandwidth of multi-ports [42, 50]. However, the most common implementation of multi-ports is referred to as six-port reflectometers (SPR) where four power detectors are used [43]. These ports are connected by a linear network upon which power detectors are strategically placed to produce a unique solution for the reflection coefficient (Fig. 1.1). The design of the linear network determines the multi-port parameters, which in return determines the sensitivity, noise immunity, and the uniqueness of the measurements. A detailed explanation of the parameter selection is provided in [40]. For a set of ill-conditioned parameters, multi-port measurements can produce multiple possible reflection coefficient values. In the current literature, SPRs are generally constructed by a combination of phase shifters, various couplers, and other microwave structures. SPRs can be implemented in both integrated circuit level [30–32, 38, 43], and board level [27, 29, 40, 41]. In [41], a multi-port is directly embedded into a distributed matching network constructed with open, and short stubs.

Additional methods that are not based on multi-ports exist for directly or indirectly measuring reflection coefficients. These methods generally rely on a directional coupler [33–35] or a circulator [36], which enables the measurement of the incident and reflected voltages directly. Another common technique is the insertion of a series element, such as an inductor [26, 55–57] or a transmission line [58] to measure the loading of the circuit. These methods generally rely on the change of voltage across the series element terminals since it is related to the loading of the circuit. These methods rely on a known physical model of the element to measure the voltage. Such an assumption is not always valid; for example, in RF and mmWave frequencies an inductor is not a simple series element, but it behaves like a two port network with series and shunt components [59].

Table 2.1: Comparison of Calibration Methods

Ref	No. Detectors	Known/Total Cal. Loads	Cal. Procedure	Meas. Procedure
[47]	4	4/4	Nonl. solv.	Nonl. solv.
[48][1]	4	≥ 7	Nonl. solv.	Nonl. solv.
[49, 51]	4	5/5	Explicit	Explicit
[50][2]	4	4/4	Explicit	Explicit
[52, 53][3]	4	3/5	Nonl. solv.	Explicit
[54]	4	1/7	Nonl. solv.	Explicit
[42][4]	3	-	-	Explicit
This work	5	3/3	Explicit	Explicit

[1] The number of calibration loads depends on the specifics of the application. This work also calibrates the power detector non-idealities using cal. loads.

[2] $|\Gamma| \approx 1$ for cal. loads

[3] $|\Gamma|$ should be equal for all cal. loads

[4] Requires high impedance detectors equally spaced on a transmission line with known Z_0. The measurement plane is set and cannot be moved. If an arbitrary measurement plane is used, at least 3 calibration loads are required.

Chapter 3

MINIMIZING THE IMPACT OF NOISE IN SIX-PORT MEASUREMENTS

In this chapter, we present a design optimization framework for N-port reflectometers that will be used in the context of built-in self-test for automotive radars. We model the error in NPR measurements due to noise and coupler gain, insertion loss, and dynamic range limitations. Based on this mathematical mode, we provide a way to select the BIST design parameters that minimize the error within the given design constraints. The proposed design framework applies to both the traditional NPR architecture that conducts the measurement in parallel and the multi-state NPR architecture that conducts the measurement in a serial fashion but with lower number of components. The mathematical model along with a numerical optimizer is verified using simulations to show that the decisions based on the model provide optimum design parameters. From this model, we select two configurations to be implemented in hardware using off-the-shelf components. Hardware experiments are conducted for the two configurations with a variety of test loads including active and passive devices. Hardware experiments show that even in the presence of components that are not characterized and in the presence of high levels of noise due to the need to use long cables, the NPR provides excellent accuracy in the context of calibration of automotive radar systems.

3.1 Noise Analysis of Six-Port Network Analyzers

In this chapter, polar coordinates will be used. The network parameters arranged in the form provided in [47] instead of using the form mentioned before (1.2). The

power incident upon each port is expressed as:

$$P_n = |B_n|^2|b|^2|1 + G_n\Gamma|^2 \tag{3.1}$$

where

$$G_n = \frac{A_n}{B_n} = g_n\angle\theta_n \tag{3.2}$$

$$\Gamma = \frac{a}{b} = \gamma\angle\phi \tag{3.3}$$

In order to make our model apply to the most general case, we use ratios of measured power as pairs, $(P_n,\ P_{c(n)})$, where $c(n)$ maps port n to its companion port. We can then choose $c(n)$ to map every port to a constant port, which would be equivalent to the measurement process in [47]. The companion port can also be unique for each port, leading to the exploration of more design alternatives.

Noise generated by each power detector needs to be taken into account to model the accuracy of the reflectometer configuration. Assuming the noise from the source is negligible compared to power detector noise, each power measurement can be expressed as:

$$P_n = |B_n|^2|b|^2|1 + G_n\Gamma|^2 + N_n \tag{3.4}$$

the noise coupled power ratio of the port pairs is defined as x_n, and can be modelled as:

$$x_n = \frac{P_n}{P_{c(n)}} = \frac{|B_n|^2|b|^2|1 + G_n\Gamma|^2 + N_n}{|B_{c(n)}|^2|b|^2\left|1 + G_{c(n)}\Gamma\right|^2 + N_{c(n)}} \tag{3.5}$$

$$= M_n\frac{1 + N_n/P_n}{1 + N_{c(n)}/P_{c(n)}} \tag{3.6}$$

Since the solution for Γ is dependent on M_n, the multiplicative term on the right hand side acts as disturbance for the overall measurement. Therefore, we define the term D_n as:

$$D_n = \frac{1 + N_n/P_n}{1 + N_{c(n)}/P_{c(n)}} \tag{3.7}$$

As we increase the incident power, $|b|^2$, the multiplicative term, D_n, nears unity, which is the ideal case. Therefore, increasing the incident power would improve the measurement accuracy as expected. The estimated Γ from measurements, $\hat{\Gamma} = \hat{\gamma}\angle\hat{\phi}$, is affected by the disturbance.

$$M_n(\hat{\Gamma}) \approx M_n(\Gamma) D_n \tag{3.8}$$

We have two options for analyzing the disturbance in (3.8). We can transform the multiplicative D_n to an additive one by taking the log of both sides, or leave it as is. Both options would result in two different cost functions. The choice of which cost function to utilize will depend on the system variables, as we will explain later.

We will first define the optimization process using the logarithm option. We take the log of both sides of (3.8):

$$\log M_n(\hat{\Gamma}) \approx \log M_n(\Gamma) + \log D_n \tag{3.9}$$

In order to numerically solve for $\hat{\Gamma}$, we propose the following cost function, which we will refer to as *log cost function*:

$$\arg\min_{\hat{\Gamma}} \sum_{i=1}^{N} \Big(\log x_n - \log M_n(\hat{\Gamma}) \Big)^2 \tag{3.10}$$

For small perturbations, M_n can be approximated as:

$$\log M_n(\hat{\Gamma}) \approx \log M_n(\Gamma) + \nabla \log M_n(\Gamma) \cdot \mathbf{\Delta\Gamma} \tag{3.11}$$

$\mathbf{\Delta\Gamma} = \begin{bmatrix} \hat{\delta_\gamma} & \hat{\delta_\phi} \end{bmatrix}^T$ signifies the distance between the estimation and the actual value, which is the measurement error. Combining (3.9) and (3.11):

$$\log(D_n) \approx \nabla \log M_n \cdot \mathbf{\Delta\Gamma} \tag{3.12}$$

The distribution of the error term is dependent on D_n and ∇M_n. Thus, optimizing the ∇M_n term enables another way of controlling the distribution of the error term. Combining the log cost function (3.10) with the (3.12) will reduce it to:

$$\arg\min_{\hat{\Gamma}} \sum_{i=1}^{N} \left(\log D_i - \nabla \log M_i \cdot \mathbf{\Delta\Gamma}\right)^2 \tag{3.13}$$

Now, we can characterize the distribution of $\mathbf{\Delta\Gamma}$ in full extent by expressing the least-squares solution for the overall system. The least square solution for $\mathbf{\Delta\Gamma}$ is given by:

$$\mathbf{N} = \mathbf{G}\mathbf{\Delta\Gamma} \tag{3.14}$$

$$\mathbf{\Delta\Gamma} = (\mathbf{G}^T\mathbf{G})^{-1}\mathbf{G}^T\mathbf{N} \tag{3.15}$$

$\mathbf{N}$ is the noise coupled measurement matrix where each row is given as $\mathbf{N}_n = \log D_n$, and $\mathbf{G}$ is the gradient matrix where each row is given as $\mathbf{G}_i = \begin{bmatrix} \nabla_{\gamma i} & \nabla_{\phi i} \end{bmatrix}$. $\nabla_{\gamma i}$ and $\nabla_{\phi i}$ represents the radial (γ) and angular (ϕ) components of $\nabla \log M_i$ in polar coordinates respectively.

$$\mathbf{G} = \begin{bmatrix} \nabla \log M_1 \\ \nabla \log M_2 \\ \vdots \\ \nabla \log M_i \\ \vdots \\ \nabla \log M_K \end{bmatrix} \tag{3.16}$$

$$\mathbf{N} = \begin{bmatrix} \log D_1 \\ \log D_2 \\ \vdots \\ \log D_i \\ \vdots \\ \log D_K \end{bmatrix} \tag{3.17}$$

$$\delta_\gamma = \frac{\sum_{i=1}^{K}\sum_{j=1}^{K}\mathbf{N}_i\left(\nabla_{\gamma i}\nabla_{\phi j}^2 - \nabla_{\phi i}\nabla_{\gamma j}\nabla_{\phi j}\right)}{\det(\mathbf{G}^T\mathbf{G})} \tag{3.18}$$

$$\delta_\phi = \frac{\sum_{i=1}^{K}\sum_{j=1}^{K}\mathbf{N}_i\left(\nabla_{\phi i}\nabla_{\gamma j}^2 - \nabla_{\gamma i}\nabla_{\gamma j}\nabla_{\phi j}\right)}{\det(\mathbf{G}^T\mathbf{G})} \tag{3.19}$$

$$\det\left(\mathbf{G}^T\mathbf{G}\right) = \sum_{i=1}^{K}\nabla_{\gamma i}^2 \times \sum_{i=1}^{K}\nabla_{\phi i}^2 - \left(\sum_{i=1}^{K}\nabla_{\gamma i}\nabla_{\phi i}\right)^2 \tag{3.20}$$

$$= 2\sum_{i=1}^{N}\sum_{j=i+1}^{N}\begin{vmatrix}\nabla\log M_i \\ \nabla\log M_j\end{vmatrix}^2 \tag{3.21}$$

If SNR is sufficiently large (i.e. SNR$\geq$20dB) and detector noise distribution is of Gaussian form, using $log(1+x) \approx x$, we can approximate the distribution of $\log D_n$ as the sum of two normal distributions.

$$\log D_n = \log(1 + N_n/P_n) - \log\left(1 + N_{c(n)}/P_{c(n)}\right) \tag{3.22}$$

$$\approx N_n/P_n - N_{c(n)}/P_{c(n)} \tag{3.23}$$

Assuming that the detector noise distributions are Gaussian and uncorrelated, and their energy is equal to σ_d^2, we can find the energy of $\mathbf{N}_i$:

$$\sigma_i^2 = \sigma_d^2\left(P_i^{-2} + P_{c(i)}^{-2}\right) \tag{3.24}$$

We define SNR as ratio of incident power to noise energy when $\Gamma = 0$:

$$SNR = \frac{\sigma_d^2}{|B_i|^2|b|^2} \tag{3.25}$$

In an application SNR would be determined by coupling gain and insertion loss and incident power.

If noise sources are correlated, or ports share companion ports (e.g. $c(n) = 0$ as in existing literature [37]), we need to add terms for accounting for the correlation. Combining (3.18), (3.19) and (3.24), we can calculate the standard deviation of γ and ϕ:

$$\sigma_\gamma = \frac{\sqrt{\sum_{i=1}^{K}\sum_{j=1}^{K}\sigma_i^2\left(\nabla_{\gamma i}\nabla_{\phi j}^2 - \nabla_{\phi i}\nabla_{\gamma j}\nabla_{\phi j}\right)^2}}{\det(\mathbf{G}^T\mathbf{G})} \tag{3.26}$$

$$\sigma_\phi = \frac{\sqrt{\sum_{i=1}^{K}\sum_{j=1}^{K}\sigma_i^2\left(\nabla_{\phi i}\nabla_{\gamma j}^2 - \nabla_{\gamma i}\nabla_{\gamma j}\nabla_{\phi j}\right)^2}}{\det(\mathbf{G}^T\mathbf{G})} \tag{3.27}$$

We will derive $\mathbf{G}$, $\mathbf{N}$ for the *linear cost function* which is defined in (3.28). It is used in almost all of the prior work and it improves performance when there is a separate reference port.

$$\arg\min_{\hat{\Gamma}} \sum_{i=1}^{N}\left(x_n - M_n(\hat{\Gamma})\right)^2 \tag{3.28}$$

We can use the following approximation for $M_n(\hat{\Gamma})$:

$$M_n(\hat{\Gamma}) \approx M_n(\Gamma) + \nabla M_n(\Gamma)\cdot\mathbf{\Delta\Gamma} \tag{3.29}$$

We combine (3.29) with (3.8):

$$M_n(\Gamma)(D_n - 1) \approx \nabla M_n \cdot \mathbf{\Delta\Gamma} \tag{3.30}$$

Thus, we can approximate $\mathbf{N}_n$ as:

$$\mathbf{N}_n = M_n(\Gamma)(D_n - 1) = \frac{N_n - M_n N_{c(n)}}{P_{c(n)} + N_{c(n)}} \tag{3.31}$$

$$\approx \frac{N_n - M_n N_{c(n)}}{P_{c(n)}} \tag{3.32}$$

Assuming the noise sources are uncorrelated, the standard deviation of $\mathbf{N}_n$ can be expressed as:

$$\sigma_i^2 = \sigma_d^2 \frac{P_n^2 + P_{c(n)}^2}{P_{c(n)}^4} \tag{3.33}$$

We can then express $\mathbf{G}$, $\mathbf{N}$ as the following:

$$\mathbf{G} = \begin{bmatrix} \nabla M_1 \\ \nabla M_2 \\ \vdots \\ \nabla M_n \\ \vdots \\ \nabla M_K \end{bmatrix} \qquad \mathbf{N} = \begin{bmatrix} M_1(\Gamma)(D_1 - 1) \\ M_2(\Gamma)(D_2 - 1) \\ \vdots \\ M_n(\Gamma)(D_n - 1) \\ \vdots \\ M_K(\Gamma)(D_N - 1) \end{bmatrix} \tag{3.34}$$

In (3.26), (3.27) by substituting, σ_i with (3.33), $\mathbf{G}$ and $\mathbf{N}$ with (3.34), we can express the distribution of the error for the linear cost function.

3.2 BIST Design Optimization

In order to minimize the error, we aim to make the rectangular distance ($\mathbf{\Delta\Gamma}$) between Γ and $\hat{\Gamma}$, as small as possible. Since we have the analytical expressions in polar coordinates, we need to convert these expressions into rectangular coordinates. The radial distance between Γ and $\hat{\Gamma}$ is δ_γ and their angular difference is δ_ϕ. Thus, the cartesian distance between Γ and $\hat{\Gamma}$ can be expressed as:

$$d(\gamma, \delta_\gamma, \delta_\phi) = \sqrt{\gamma^2 + (\gamma + \delta_\gamma)^2 - 2\gamma(\gamma + \delta_\gamma)\cos\delta_\phi} \tag{3.35}$$

$$\approx \sqrt{\delta_\gamma^2 + \gamma^2 \delta_\phi^2} \tag{3.36}$$

If $p(x, \sigma)$, defined as the probability density function (PDF) of a normal distribution with zero mean and standard deviation of σ, we can express the expected value of

the cartesian distance of a given point $\Gamma = \gamma\angle\phi$ as:

$$d_{avg}(\gamma,\phi) = \int_{-\infty}^{+\infty}\int_{-\infty}^{+\infty} d(\gamma,\delta_\gamma,\delta_\phi)p(\delta_\gamma,\sigma_\gamma)p(\delta_\phi,\sigma_\phi)\,\mathrm{d}\delta_\gamma\,\mathrm{d}\delta_\phi \tag{3.37}$$

Even though δ_γ and δ_ϕ are correlated, we found the correlation coefficient between these parameters is too small to make a discernible difference. Therefore, we separate the distributions as if they were uncorrelated. If we want to account for the correlation between these terms, we can use bivariate normal distribution instead of multiplying two normal distributions. We also found that the following approximation for d_{avg} also works quite well (Fig. 3.1), which can be used to speed up the computations.

$$d_{avg}(\gamma,\phi) \approx \sqrt{\sigma_\gamma^2 + \gamma^2\sigma_\phi^2} \tag{3.38}$$

Since σ_γ and σ_ϕ are dependent on a given point, we integrate (3.37) over the region of interest (generally the unit circle) to find the mean distance between Γ and $\hat{\Gamma}$, which is the average error of the measurement system, using:

$$MD = \frac{1}{2\pi}\int_0^1\int_0^{2\pi} d_{avg}(\gamma,\phi)\,\mathrm{d}\phi\,\mathrm{d}\gamma \tag{3.39}$$

We want to emphasize that minimizing (3.39) using the given definition of d would just minimize the average distance between Γ and $\hat{\Gamma}$. Depending on the design goal and application, we also might to minimize the ratio of $|\Gamma - \hat{\Gamma}|/|\Gamma|$. In that case, we need to divide (3.37), (3.38) by $|\Gamma| = \gamma$.

In summary, to decrease the error in the measurements, we need to decrease the detector noise σ_d, increase the incident power to detectors $|B_i|^2|b|^2$, or choose parameters G_i such that it would minimize (3.39). Since the first two are generally limited by the application constraints, such as area, coupler insertion loss, or energy consumption, we will focus on choosing parameters G_i.

Since the expanded forms of (3.37) and (3.39) are not analytically tractable, we will provide qualitative arguments for a possible set of constraints on parameters and employ numerical methods for finding the optimum set of parameters for the given constraints.

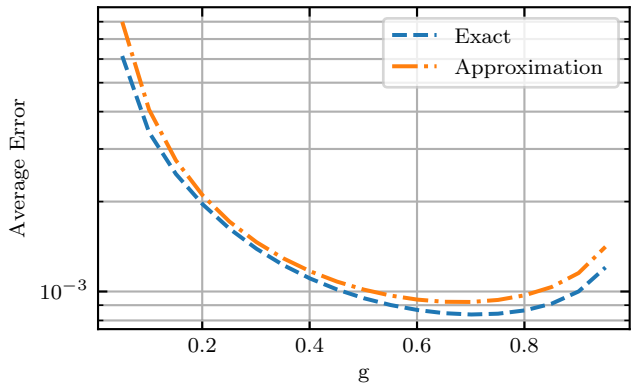

Figure 3.1: Average Error using Exact (3.37) vs Approximate (3.38) d_{avg} for $(6, 2)$

3.3 Dynamic Range

In a BIST application, the dynamic range of the power detectors is typically limited. Moreover, the incident power will be limited due to output power constraints as well as the gain of the coupler that routes the incident signal to the phase shifter. Thus, power limitations can be due to maximum input power of the DUT, linear region of the power detector, and noise floor. Given this dynamic range, during BIST design, we need to limit the range of P_ns in an interval. We can find this interval by using the triangle inequality.

$$|1 - |G_n\Gamma||^2 < |1 + G_n\Gamma|^2 < 1 + |G_n||\Gamma| \tag{3.40}$$

$$1 - g_n\gamma_{max} < |1 + G_n\Gamma|^2 < 1 + g_n\gamma_{max} \tag{3.41}$$

Since, interval of the values that P_n can take determined by g_i and Γ, following equation can be used for finding g value given the dynamic range (k) and $\gamma_{max} =$

max$|\Gamma|$.

$$k = \frac{P_{in(max)}}{P_{in(min)}} = \frac{1 + g_i\gamma_{max}}{1 - g_i\gamma_{max}} \tag{3.42}$$

This result can be used for setting boundaries on a numerical solver. Since we are interested in optimum parameters in the unit circle, $\gamma_{max} = 1$, we set the following constraint on g_i:

$$0 < g_i \leq 1 \tag{3.43}$$

We need to set one of the ports as *phase reference*. Without loss of generality, we choose $\theta_1 = 0$. Moreover, since increasing energy coupled to detectors does not degrade any other performance metric, we can maximize $|B_i|^2|b|^2$ as much as the application permits. In the rest of chapter, we just select $|B_i|^2|b|^2 = 1$.

In order to simplify the analysis, we will set the magnitude of the parameters $g = |G_n|$ and the angle separation between consecutive parameters to be equal as a design goal. While deviations from this design goal due to process variations will be taken into account during the calibration process, equal magnitude and phase separation also is the optimum design point for any NPR without any constraints.

$$\theta_{n+1} = \theta_n + \theta \tag{3.44}$$

We need to keep (3.24) as small as possible. Therefore, when P_n reaches its smallest value, we want to make its companion, $P_{c(n)}$, as large as possible. Based on (3.40), placing their angles 180° apart would accomplish that.

Thus:

$$\theta_n - \theta_{c(n)} = \pi \tag{3.45}$$

3.4 Optimum Parameters

To obtain an initial point for the optimum solution, we apply (3.45) as a known. Furthermore, since the error due to noise increases as the magnitude of γ decreases,

we set we set $\gamma = 0$ as the worst case. This reduces the $\det\left(\mathbf{G}^T\mathbf{G}\right)$ to following:

$$\det\left(\mathbf{G}^T\mathbf{G}\right) = 512g^4 \sum_{m=1}^{K} \sum_{j=m+1}^{K} sin(\theta_n - \theta_m)^2 \tag{3.46}$$

If we select $\theta_1 = 0$, the angles that maximize this function are:

$$\theta_n = (n-1)\frac{\pi}{K} \tag{3.47}$$

where $n = 1, 2, ..., N-2$ is the number of the measurement port and K=2, 3, 4. In a similar manner, if we let $c(n) = 0$ and $G_0 = 0$, we can calculate $\det\left(\mathbf{G}^T\mathbf{G}\right)$, for various design points. For instance, for $N = 6$:

$$\det\left(\mathbf{G}^T\mathbf{G}\right) = 32g^4(cos(2\theta) + 2)sin(\theta)^2 \tag{3.48}$$

and for $N = 7$:

$$\det\left(\mathbf{G}^T\mathbf{G}\right) = 16g^4(-8\sin^4(\theta) + 11\sin^2(\theta) + \sin^2(3\theta)) \tag{3.49}$$

We expect the angle separation for these cases occur at maximums, therefore from (3.48) we expect separation for $N = 4$ to be either 60°, 120° and for $N = 5$ we expect angle separation to be one of the following angles 45°, 90° or 135°. These intuitive values are confirmed by optimizing for minimum error (i.e. minimum distance between Γ and $\hat{\Gamma}$) using a numerical solver. Using Limited-memory BFGS algorithm (L-BFGS-B) [60], we minimized the mean distance given in (3.39) over the unit circle, and found the values given in Table 3.1.

In Table 3.1, N corresponds to the number of ports, where the number of power detectors is $N - 2$. K corresponds to number of M_i components.

In the $(6, 2)$ configuration, every port has a companion port such that $G_n/G_{c(n)} = -1$, and successive ports are separated by 90°, i.e., $G_{n+1}/G_n = j$. The prior work [37] corresponds to the $(6, 3)$ configuration. In this configuration, there are 3 measurement axes and each axis shares the same companion (reference) port. The model

Table 3.1: Optimum Parameters for Average Error

N	K	Average Distance		Average Distance Ratio	
		g	***Separation*** (θ)	***g***	***Separation*** (θ)
6^1	2	0.71	90°	0.86	90°
8^1	3	0.66	60°	0.84	60°
10^1	4	0.62	45°	0.82	45°
6^2	3	1.00	120°	1.00	120°
7^2	4	1.00	90°	1.00	90°

[1] $c(n) = K + n$

[2] $c(n) = 0$, $G_0 = 0$ constraint to replicate [37]

for this configuration is thoroughly examined in [37] but the author did not provided a rigorous proof for the design criteria. By applying the analysis developed in this work for this configuration, we find that the optimum angle separation between parameters (θ) to be 120°, which was the intuitive result in [37]. The optimum angle separations given in Table 3.1 are also consistent with our initial intuitive estimates that maximize $\det(\mathbf{G}^T\mathbf{G})$. With these results, we surmise that other terms involved in the expressions (3.26) and (3.27) determine the optimal g values, while $\det(\mathbf{G}^T\mathbf{G})$ determines the angle separation.

Depending on the application, we may want to minimize the number of power detectors, due to the area and energy constraints. Moreover, we found that the effect of increasing the number of power detectors on accuracy is almost negligible. Therefore, even though there are many possible configurations, we can limit our discussion on $(6, 2)$, $(6, 3)$ and $(7, 4)$ configurations.

Even though the $(7, 4)$ configuration has more power detectors than the others, its

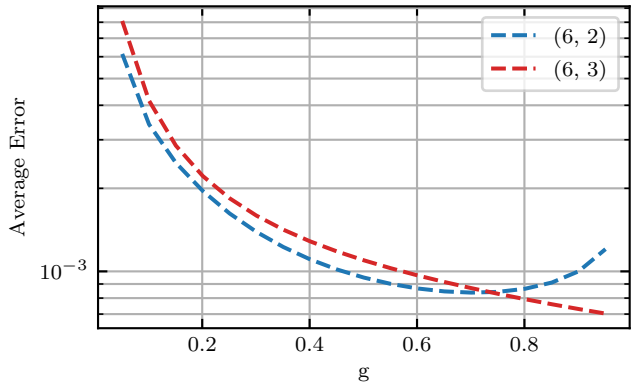

Figure 3.2: Comparison of $(6, 2)$ and $(6, 3)$

parameters are separated by 90°, which makes it more attractive for some applications, specifically the applications that require wideband operation [43]. As can be seen in Fig. 3.3, the average error of the $(7, 4)$ configuration is very close to the $(6, 3)$ configuration. In these two configurations, the error can be reduced by making g larger (Fig. 3.3). This trend does not hold for the $(6, 2)$ configuration. The primary reason of this is for $g > 1$, there are multiple solutions for Γ in the $(6, 2)$ configuration.

Configurations $(6, 2)$ and $(7, 4)$, have good qualities that make them attractive for practical applications. These configurations yield integer multiples of 90° as separation between power detectors. Thus, one can achieve wider bandwidth with this configuration compared to the $(6, 3)$ configuration which needs 120° separation. Also, unlike 120° phase shift, a 90° phase shift can be obtained by the natural behavior of the components.

The $(6, 2)$ configuration also becomes handy if an application does not permit using a directional coupler (e.g. ICs). Since in the $(6, 2)$ configuration, all $|G_n|$ values are equal and larger than 0, one can just place power detectors along a transmission line, and measure Γ without employing any directional couplers (similar to [30, 42]), which is a required for the prior work [37]. Another important result that can be deduced from Fig. 3.3 and 3.2, is that if one can choose arbitrary large g values, using

a directional coupler to define a *reference port* is the best solution. This would also require power detectors with a wide dynamic range. However, increasing g beyond 0.6 provides diminishing returns in terms of accuracy. Thus, wide-dynamic range power detectors generally are not necessary. Moreover, since adding one more power detectors does not increase accuracy substantially, using the $(6, 3)$ configuration instead of the $(7, 4)$ configuration would be more desirable, assuming that a 90° separation between parameters is not required.

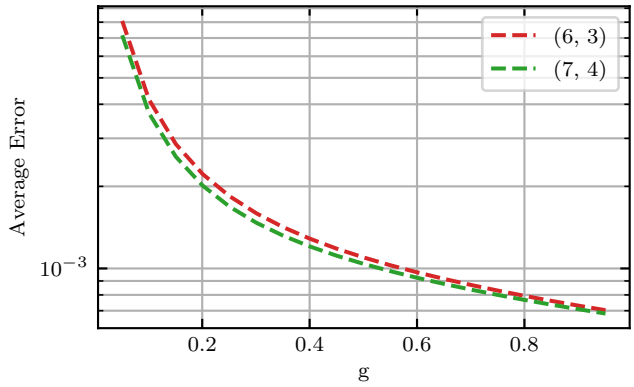

(a) $g < 1$

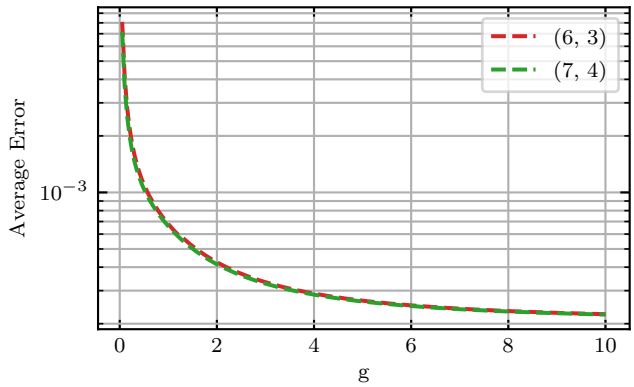

(b) $g < 10$

Figure 3.3: Comparison of $(6, 3)$ and $(7, 4)$

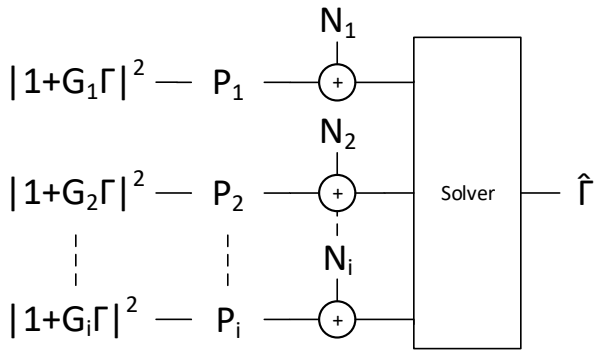

Figure 3.4: Simulation Flow

3.5 Simulation Results

To verify our mathematical model for the average error (3.39), we performed simulations as described in Fig. 3.4. We first set arbitrary Γ values to mimic the device under test. We then simulate the power at each detector after adding noise with an SNR of 30dB, for different g values. The measured power values are fed into the solver for the estimation of $\hat{\Gamma}$.

Fig. 3.2 compares the estimation error for the $(6, 2)$ and $(6, 3)$ configurations. This figure provides an interesting design choice. We found that if the BIST system is limited by $g < 0.8$ due to splitter and combiner losses as well as the coupling gain (which is typically negative), that the $(6, 2)$ configuration provides more accurate results than the $(6, 3)$ configuration. We also compared different cost functions (3.10) and we found log-cost function improved the system accuracy for certain scenarios. As can be seen from Fig. 3.6, for $(6, 3)$ configuration, if $g < 0.65$ log cost function provides slightly better accuracy.

There is a small difference between simulations and the model, this can be attributed to (3.8), where the estimated noise incorporated in the multiplication factor, D_n, leaves a small additive residue. This residue may cause inconsistent solutions for

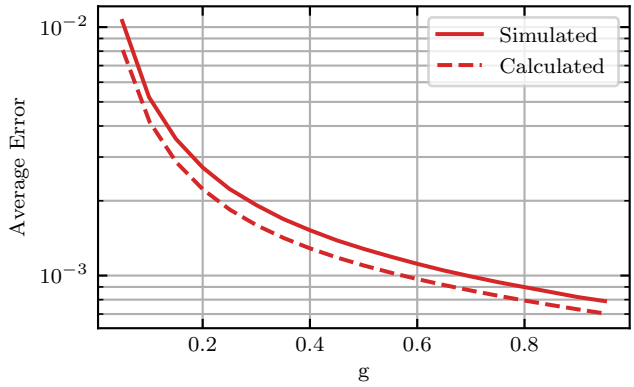

(a) Comparison of Simulated and Calculated Average Error for $(6, 3)$

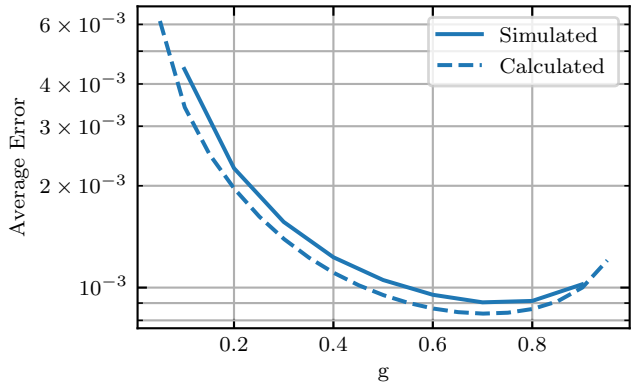

(b) Comparison of Simulated and Calculated Average Error for $(6, 2)$

Figure 3.5: Comparison of Simulated and Calculated Average Error

$\hat{\Gamma}$ and its corresponding $M_n(\hat{\Gamma})$. In other words, the solutions that are determined by the numerical solver may not converge to the precise location of Γ. Since the noise residue has similar distribution (zero mean, Gaussian), it effectively will lower the SNR. Therefore, the model will have a lower bound for the average error. However, the majority of the impact of noise is included in the model and as shown in Fig. 3.5, the predicted error by the mathematical model closely matches the error from the simulations. It should be noted that the small difference in estimated error via the mathematical model and the simulation-based model does not result in any wrong decisions. The optimum choice of BIST parameters, in terms of available gain and

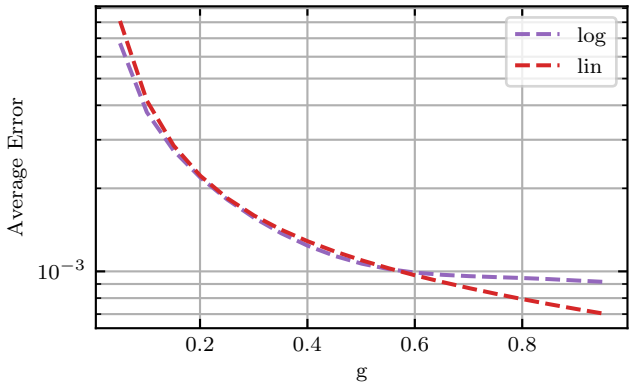

Figure 3.6: Comparison of log and lin Cost Functions for $(6, 3)$ Configuration

dynamic range are identical whether the proposed mathematical analysis is used or the decision is entirely based on simulations (which is not tractable due to the large design space).

3.6 Multi-state Reflectometer Implementation

In order to decrease the number of required components, structure shown in Fig. 3.8 can be used. In this structure, instead of multiple fixed phase shifters, a variable

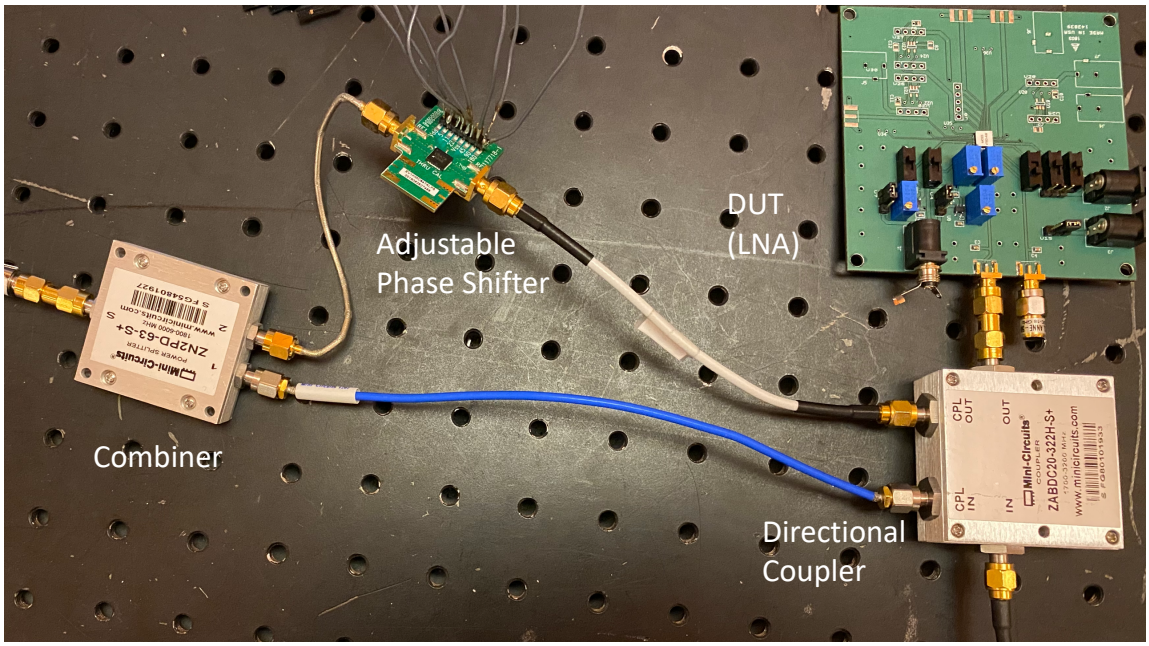

Figure 3.7: Experiment Setup

phase shifter is used. We do not need to know the phase shift amount nor they need to be spaced equally, since we can find these values with calibration. But the phase shift provided by the phase shifter should be repeatable and should have enough range for extracting linearly independent information. In other words, the variable phase shifter should be designed to cover the range for process and dynamic variations for the device under test. If in an application phase shifter cannot provide the ideal values, expected error can be found by using analysis provided in the previous subsection.

The phase shifter is placed on the signal path that is most closely related to the reflected signal from the DUT. This configuration will take advantage of the inherent loss of the phase shifter and limit the g value. The phase shifted signal is combined with the signal that is predominantly function of the incident signal. The measured power is related to the Γ of the device under test as described in (3.1).

The measurement is conducted in multiple steps. In each step, phase shifter is set to a different angle and the ratio of the measurements from the power detectors are recorded. After all measurement results are recorded, Γ can be solved for using the same process as defined before.

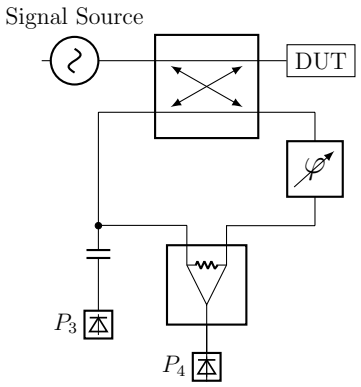

Figure 3.8: Multi-state Reflectometer Structure

Generally, the phase shifter also introduces attenuation to the signal, which would make $g < 1$. This attenuation level is typically sufficient to set g to a reasonable value.

If the g value needs to be further reduced, additional attenuators can be used.

One potential problem with power detectors is their measurement does not contain frequency and phase information. Therefore, they are susceptible to interference when used in-field. To overcome this, test signal can be modulated, even a basic on-off keying would suffice to separate test signal from the interference as shown in [61].

3.7 Hardware Experiments to Verify Proposed Design

In order to demonstrate the feasibility of using NPR as a BIST solution, we have built two configurations, the $(6, 2)$ and the $(7, 4)$ configurations, using off-the-shelf components. While we use discrete components, these components are not pre-characterized; their imperfections are taken into account during the NPR calibration process. The experimental configurations are similar to multistate reflectometer presented in Fig. 3.8 with the number of phase shift and measurement operations being the difference between the configurations. A picture of the experimental set-up, which consists of a directional coupler (Mini-Circuits ZABDC20-322H-S+), a digitally adjustable phase shifter (HMC647A), and a power combiner (ZN2PD-63-S+), is shown in Fig. 3.7. Four passive calibration loads are used to determine BIST network parameters, as in prior work [47]. For test loads, we have used 8 passive devices consisting of passively terminated SMA connectors, and an LNA. In practice, the loads that we intend to measure with the BIST will be more closely clustered, making the design and calibration process easier.

We performed the measurements as described before. By setting phase shifter to $0°$, $90°$, $180°$, and $270°$, and recording the ratio of incident power to power at the output port, we were able to measure Γ of the DUT for different loads and frequencies. The results from the NPR built from off-the-shelf components are compared with measurements using a high-end RF equipment, Agilent E8361A Vector Network

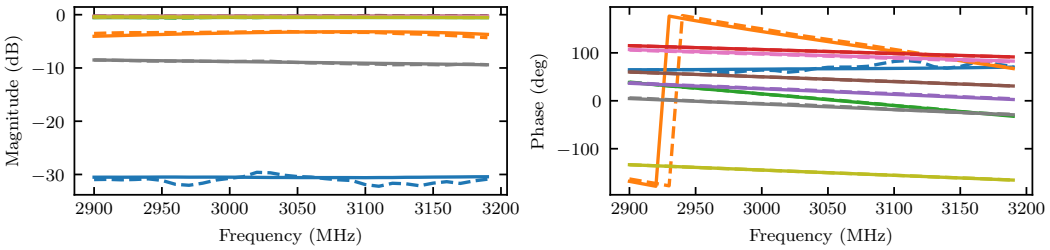

(a) (7, 4)

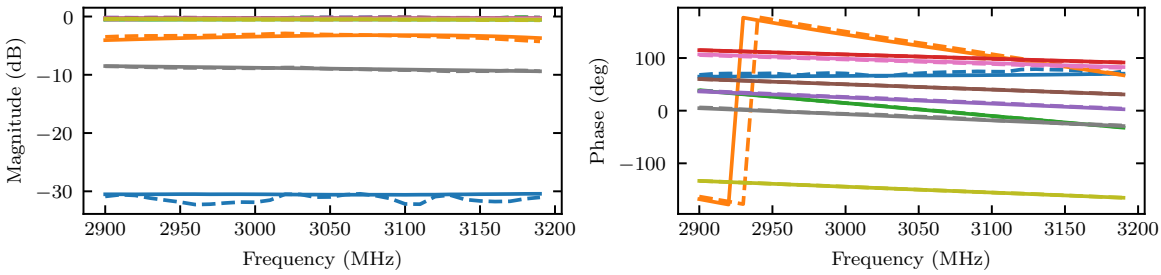

(b) (6, 2)

Figure 3.9: Comparison of VNA (Solid Line) based characterization of the reflection coefficient to the proposed NPR based characterization (Dashed Line) for the two implemented configurations. Blue: 50 Ω, Orange: LNA, Green: 100 Ω, Cyan: Shorted SMA, otherwise: Open TLINs with different lengths

Analyzer. The test load results for the $(7, 4)$ configuration are shown in Fig. 3.10 and the test load results for the $(7, 4)$ configuration are shown in Fig. 3.11.

The comparison of measurements on the Smith Chart in Fig. 3.10 and Fig. 3.11 show that the NPR results are very close to that of the VNA for a variety of loads, active and passive. Fig. 3.9 shows the same comparison in magnitude-phase plots. Table 3.2 shows the average error over the six test loads that are used for the two BIST configurations. As discussed in Section 3.2, the error is defined as the vector magnitude between the actual and estimated location of the reflection coefficient in the Cartesian space as compared with the magnitude of the reflection coefficient. The two configurations provide similar accuracy at ($g = 0.6$) as predicted by the mathematical model. Thus, depending on the availability of phase shifters and the

Table 3.2: Experiment Summary

Configuration	Measurements	
	g	***Avg. Error***
(6, 3)	0.6	0.020
(7, 4)	0.6	0.016

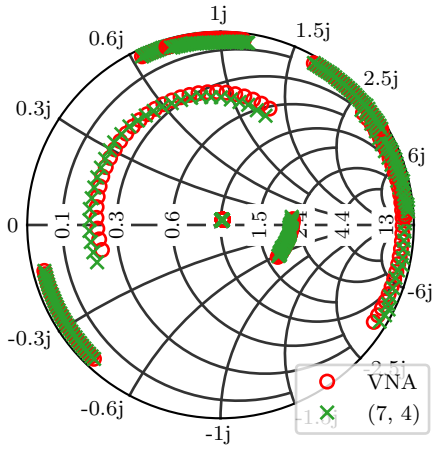

Figure 3.10: Comparison of the reflection coefficient characterization via the NPR using the (7, 4) configuration to the VNA characterization

number of measurements that can be conducted, either configuration can be selected. We have also evaluated the impact of this level of error in the context of calibration of automotive radar. We have found through system-level simulations [62] that this measurement error has virtually no impact on the overall accuracy of the radar in terms of angle, speed, or range. In other words, if the system is calibrated with respect to this measurement result, it will provide the expected resolution in terms of these three variables.

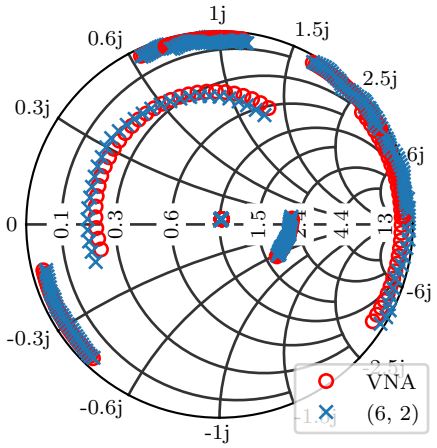

Figure 3.11: Comparison of the reflection coefficient characterization via the NPR using the (6, 2) configuration to the VNA characterization

Chapter 4

PERIODIC STRUCTURES AS SIX-PORTS

In this chapter, a new multi-port architecture that uses periodic structures is proposed. This new structure results in a new model for multi-ports, which greatly simplifies equations. This simplification results in closed-form calibration and measurements for the multi-ports. Also, calibration can be done by just using three loads, which was not possible in generic SPR architectures. The proposed theory is verified with Monte-Carlo, circuit, and EM simulations. Experimental results show that the proposed method gives excellent accuracy for a wide range of frequencies and loads.

4.1 Periodic Structures

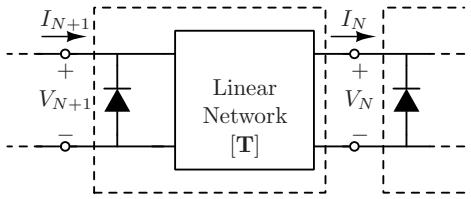

Figure 4.1: Unit cell of a Periodic Structure

Multi-ports are generally analyzed and modeled with scattering parameters. However, due to the repeating nature of the proposed structure, using ABCD/transmission parameters and measuring loads in the admittance domain (at least initially) simplifies the analysis.

Voltages and the currents at the ports of the unit cell (Fig. 4.1) are related through the unit cell's transmission matrix. This relation can be described as:

$$\begin{bmatrix} V_{N+1} \\ I_{N+1} \end{bmatrix} = \begin{bmatrix} A & B \\ C & D \end{bmatrix} \begin{bmatrix} V_N \\ I_N \end{bmatrix}. \tag{4.1}$$

Let $\mathbf{T}$ denote the transmission matrix of the unit cell:

$$\mathbf{T} = \begin{bmatrix} A & B \\ C & D \end{bmatrix}. \tag{4.2}$$

The voltage and current at any port in the periodic structure (Fig. 4.2) can be found by using the cascading property of the transmission matrices, as the following:

$$\begin{bmatrix} V_N \\ I_N \end{bmatrix} = \mathbf{T}^N \begin{bmatrix} V_0 \\ I_0 \end{bmatrix}. \tag{4.3}$$

The relation between I_0 and V_0 in terms of the measured admittance $Y = Z^{-1}$ can be expressed as:

$$I_0 = V_0 Y. \tag{4.4}$$

I_N can be expressed in terms of V_N and Y by multiplying both sides of (4.3) by $1/V_0$ and using (4.4) as:

$$\begin{bmatrix} V_N/V_0 \\ I_N/V_0 \end{bmatrix} = \mathbf{T}^N \begin{bmatrix} 1 \\ Y \end{bmatrix}. \tag{4.5}$$

Observe that N can be a positive or negative integer. This observation will be used to simplify the formulation and derive explicit calibration and measurement procedures.

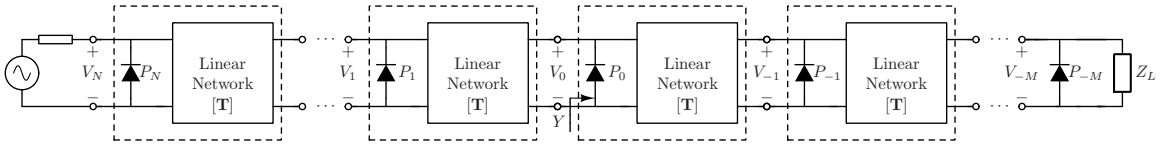

Figure 4.2: Proposed Measurement System

4.2 Reciprocal Cells with Diagonalizable Matrices

The transmission matrix can be used for modeling all two-port linear circuits. This work will concentrate on linear circuits that are reciprocal and have a diagonalizable

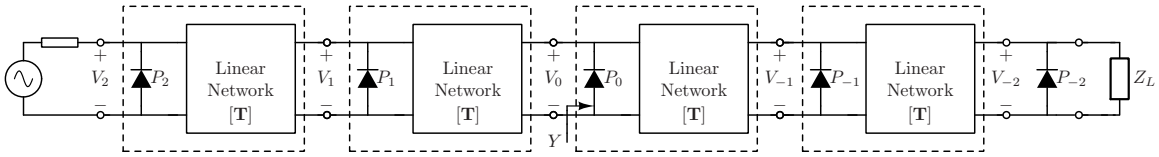

Figure 4.3: Five detector implementation of the proposed method

transmission matrix (**T**). In RF frequencies, most components, such as inductors, belong to this category. If an element has a series and a shunt component, it likely has a diagonalizable transmission matrix (see next section for more details).

If matrix **T** is diagonalizable, it can be written as:

$$\mathbf{T}^N = \mathbf{Q}\mathbf{\Lambda}^N\mathbf{Q}^{-1}. \tag{4.6}$$

For any 2x2 matrix, **Q** can be written as:

$$\mathbf{Q} = \begin{bmatrix} v_1 & v_2 \\ 1 & 1 \end{bmatrix} \tag{4.7}$$

where $\mathbf{v}_{1,2} = \begin{bmatrix} v_{1,2} & 1 \end{bmatrix}^T$ are eigenvectors of **T**. Similarly, $\mathbf{\Lambda}$ can be written as:

$$\mathbf{\Lambda} = \begin{bmatrix} \lambda_1 & 0 \\ 0 & \lambda_2 \end{bmatrix} \tag{4.8}$$

where $\lambda_{1,2}$ are eigenvalues of **T**. For reciprocal circuits $\det \mathbf{T} = \lambda_1\lambda_2 = 1$. Let $\lambda = \lambda_1$, then the matrix can be expressed as:

$$\mathbf{T}^N = \frac{1}{v_1 - v_2} \begin{bmatrix} v_1 & v_2 \\ 1 & 1 \end{bmatrix} \begin{bmatrix} \lambda^N & 0 \\ 0 & \lambda^{-N} \end{bmatrix} \begin{bmatrix} 1 & -v_2 \\ -1 & v_1 \end{bmatrix}. \tag{4.9}$$

Putting (4.9) in (4.5); normalized voltages are expressed in terms of the eigenvalues, eigenvectors, and load admittance as:

$$\frac{V_N}{V_0} = \frac{\lambda^N\left(-Yv_1v_2 + v_1\right) + \left(Yv_1v_2 - v_2\right)\lambda^{-N}}{v_1 - v_2}. \tag{4.10}$$

Let $v_2 = kv_1 = kv$, then the normalized voltage becomes:

$$\frac{V_N}{V_0} = \frac{\lambda^N (Yvk - 1) + k (1 - Yv) \lambda^{-N}}{k - 1}. \tag{4.11}$$

Let $w = (Yvk - 1)/(k - 1) - 1/2$, then the normalized voltage can be expressed as:

$$\frac{V_N}{V_0} = \lambda^N \left(\frac{1}{2} + w\right) + \lambda^{-N} \left(\frac{1}{2} - w\right). \tag{4.12}$$

From (4.12), one can observe that, each introduced measurement port is linearly independent and does not increase the number of unknowns. This central finding is key to reducing the number of the calibration loads and computational complexity. Note that the load of interest Y is a bilinear transform (Möbius transform) of the w, therefore after w is measured, Y can be solved in terms of w. This will be investigated in the calibration section.

4.3 Unit Cells with Diagonalizable Transmission Matrix

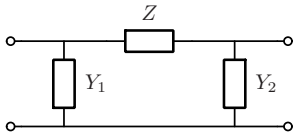

Figure 4.4: π-network representation of a reciprocal two-port linear network

Any reciprocal linear network can be modeled as the circuit given in Fig. 4.4. Z, Y_1 and Y_2 values can be calculated using Y-parameters. Given Z, Y_1 and Y_2, the transmission matrix of this unit cell is:

$$\mathbf{T} = \begin{bmatrix} Y_2Z + 1 & Z \\ Y_1 + Y_1Y_2Z + Y_2 & Y_1Z + 1 \end{bmatrix}. \tag{4.13}$$

The eigenvalues of this matrix are:

$$\lambda_{1,2} = 1 + \frac{Z(Y_1 + Y_2) \pm \sqrt{Z (Y_1 + Y_2) (Z(Y_1 + Y_2) + 4)}}{2}. \tag{4.14}$$

Therefore, if the following conditions are met:

- There is a series element in the equivalent circuit ($Z \neq 0$)
- There is at least one shunt element in the equivalent circuit, and the sum of the admittance of the shunt elements is not zero ($Y_1 + Y_2 \neq 0$)
- Multiplication of the series element impedance and the sum of the admittance of the shunt elements satisfies the following $Z(Y_1 + Y_2) + 4 \neq 0$

The transmission matrix of the unit cell will be diagonalizable.

4.4 Power Detector Measurements

To solve for w, power detector/voltage measurements can be used. It is assumed that λ is known and found by calibration. After w is found, an error-box correction approach can be used to find the load value explicitly. Error-box parameters also will be found during the calibration phase.

The output of each power detector can be formulated as:

$$P_N = g|V_N|^2 \tag{4.15}$$

where g is the gain of the power detector. Power measurements will be normalized by a predetermined "reference" power measurement to cancel out the detector gains and the scaling effects of the test signal amplitude. Therefore, the measurement ratio (M_N) is defined as:

$$M_N = \frac{P_N}{P_0} = \left|\frac{V_N}{V_0}\right|^2 \tag{4.16}$$

where V_0 is the reference voltage measurement. To find an explicit formulation, (4.12) needs to be rearranged as the following:

$$M_N = \left|\frac{V_N}{V_0}\right|^2 = \left|(\lambda^N - \lambda^{-N})w + \frac{1}{2}(\lambda^N + \lambda^{-N})\right|^2. \tag{4.17}$$

Let $J_N = \lambda^N - \lambda^{-N}$ and $L_N = \lambda^N + \lambda^{-N}$, then M_N can be expressed as:

$$M_N = |J_N|^2|w|^2 + \frac{1}{4}|L_N|^2 + \mathrm{Re}\{J_N L_N^* w\} \tag{4.18}$$

and M_{-N} can be expressed as:

$$M_{-N} = |J_N|^2|w|^2 + \frac{1}{4}|L_N|^2 - \mathrm{Re}\{J_N L_N^* w\}. \tag{4.19}$$

This symmetry can be used to separate the terms as follows:

$$A_N = M_N + M_{-N} = 2|J_N|^2|w|^2 + \frac{1}{2}|L_N|^2 \tag{4.20}$$

$$B_N = M_N - M_{-N} = 2\,\mathrm{Re}\{J_N L_N^* w\}. \tag{4.21}$$

These concepts and definitions will be used later in the calibration section as well. If λ (therefore J_N and L_N is known), $|w|$ can be expressed as:

$$|w|^2 = \frac{A_N - 0.5|L_N|^2}{2|J_N|^2}. \tag{4.22}$$

Similarly, $\mathrm{Re}\{J_N L_N^* w\}$ can be expressed as:

$$\mathrm{Re}\{J_N L_N^* w\} = \frac{B_N}{2}. \tag{4.23}$$

Using λ, $|w|$ and $\mathrm{Re}\{J_N L_N^* w\}$, the imaginary part can be expressed as:

$$\mathrm{Im}\{J_N L_N^* w\} = \pm\sqrt{|J_N L_N|^2|w|^2 - \mathrm{Re}^2\{J_N L_N^* w\}}. \tag{4.24}$$

Finally, from the measurements, two possible solutions for w are found:

$$w_{1,2} = \frac{\mathrm{Re}\{J_N L_N^* w\} \pm j\,\mathrm{Im}\{J_N L_N^* w\}}{J_N L_N^*}. \tag{4.25}$$

So far, only two measurements are used. At least one more measurement (i.e., $N+1$) is necessary to find the correct root. Therefore, at least three measurements (four power detectors) are needed to find w unambiguously. The correct solution can be

selected by plugging values back in (4.17) and choosing the solution that has the smallest difference between the predicted and actual power measurement. This final measurement step can be expressed as:

$$\underset{w\in\{w_1,w_2\}}{\arg\min}\left|M_{N+1}-\left|\lambda^2\left(\frac{1}{2}+w\right)-\lambda^{-2}\left(\frac{1}{2}-w\right)\right|^2\right|. \tag{4.26}$$

After w is solved, the calibration and system information can be used to extract Y, Z or Γ. The given formulations are correct for any N. Due to its convenience and ease of calculation $N = 1$ is selected. Therefore; M_{-1}, M_1, M_2 will be used for calculating w.

4.5 Calibration

The calibration procedure will be performed in two steps. In the first step, λ will be found. After λ is known, three distinct loads can be used to find the bilinear relationship between w and the load Z_L (Fig. 4.3).

The notation introduced before is expanded to accommodate for the different calibration loads. For load i, the measurement expression is given as:

$$M_{Ni} = |J_N|^2|w_i|^2+\frac{1}{4}|L_N|^2+\operatorname{Re}\{J_N L_N^* w_i\}. \tag{4.27}$$

Similarly, A_{Ni}, B_{Ni} can be expressed as:

$$A_{Ni} = M_{Ni} + M_{-Ni} = 2|J_N|^2|w_i|^2+\frac{1}{2}|L_N|^2 \tag{4.28}$$

$$B_{Ni} = M_{Ni} - M_{-Ni} = 2\operatorname{Re}\{J_N L_N^* w_i\}. \tag{4.29}$$

For simplicity, assume that there are five power detectors, and they are arranged as shown in Fig. 4.3. Then, for load i, there will be four measurements (M_{-2i}, M_{-1i}, M_{1i}, M_{2i}).

Initially, measurements for two different loads $i = 1, 2$ are used for finding λ, which is expressed in polar coordinates $\lambda = re^{j\theta}$. The quantities that can be calcu-

lated/inferred from the measurements are denoted as W_m, to differentiate between known quantities from unknown quantities up to that point.

First, observe that $J_2 = J_1 L_1$. Based on this $|L_1|^2$ can be found by:

$$W_1 = \frac{A_{2,1} - A_{2,2}}{A_{1,1} - A_{1,2}} \tag{4.30}$$

$$= |L_1|^2. \tag{4.31}$$

which in turn can be expressed in polar coordinates:

$$W_1 = r^2 + r^{-2} + 2\cos 2\theta. \tag{4.32}$$

Using $W_1 = |L_1|^2$, the following can be found:

$$W_1 A_{1,1} - A_{2,1} = \frac{|\lambda - \lambda^{-1}|^4 - |\lambda^2 - \lambda^{-2}|^2}{2} \tag{4.33}$$

$$= 2\cos 2\theta (r^2 + r^{-2}) + 2. \tag{4.34}$$

Let W_2 be:

$$W_2 = \frac{W_1 A_{1,1} - A_{2,1} - 2}{2} \tag{4.35}$$

$$= \cos 2\theta (r^2 + r^{-2}) \tag{4.36}$$

by using W_1 and W_2, $\cos 2\theta$ can be found by solving:

$$0 = 2\cos^2 2\theta - W_1 \cos 2\theta + W_2. \tag{4.37}$$

There are two roots in this equation. One of the roots corresponds to $\cos 2\theta$, and the other root corresponds to $(r^2 + r^{-2})/2$. This fact also can be verified by observing that the product of the roots of this equation is equal to $W_2/2 = \cos 2\theta (r^2 + r^{-2})/2$. Luckily, the roots can be assigned to the corresponding expressions unambiguously by observing that $(r^2 + r^{-2})/2 \geq 1$ and $\cos 2\theta \leq 1$, as the following:

$$\cos 2\theta = \frac{W_1 - \sqrt{W_1^2 - 8W_2}}{4} \tag{4.38}$$

$$W_3 = r^2 + r^{-2} = \frac{W_1 + \sqrt{W_1^2 - 8W_2}}{2}. \tag{4.39}$$

Using W_3, (4.39) can be succinctly expressed as:

$$0 = r^4 - W_3 r^2 + 1. \tag{4.40}$$

By solving this equation, all possible solutions for the r are found:

$$r = \pm\sqrt{\frac{W_3 \pm \sqrt{W_3^2 - 4}}{2}}. \tag{4.41}$$

As expected, there are four roots for this equation and they correspond to $\pm r, \pm 1/r$. The sign of the r does not matter, because only r^2 term is used in the measurements. $1/r$ is also a valid solution since there are two eigenvalues and they are inverse of each other. Both eigenvalues will produce valid and correct measurements.

The only term that cannot be solved unambiguously is the imaginary part of λ. To solve it unambiguously, the sign of $\sin 2\theta = \pm\sqrt{1 - \cos^2 2\theta}$ needs to be determined, which is not possible with the given calibration procedure. In practice, this is not a big concern since the sign of this expression is related to the intrinsic properties of the unit cell. Therefore, the sign can be determined *a priori*. In the cases where this is not feasible, a fourth load can be used as a test load to determine the sign. If the fourth load measurement does not correspond to the known value, the imaginary sign is changed, and measurement is performed again. This completes the first step of the two-step calibration.

In the second step, error-box parameters that relate w to Z_L will be solved (Fig. 4.5). Now, that λ is solved, w_i for each load can be measured as described in the previous section. Each w_i is a bilinear transform of Y_i, which in return is a bilinear

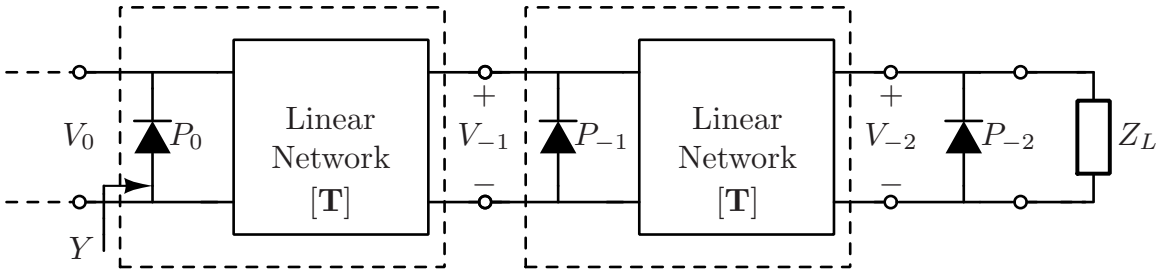

(a) Measurement Plane

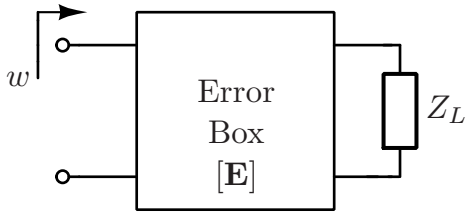

(b) Error Box Equivalent

Figure 4.5: Transformation Steps Demonstrating $Y \mapsto w \mapsto Z_L$

transform of the load of interest Z_{Li}. The composition of bilinear transforms is a bilinear transform. Therefore, there exists a bilinear relationship between w_i and Z_{Li}, which can be expressed as:

$$Z_{Li} = \frac{aw_i + b}{cw_i + 1}. \tag{4.42}$$

Using three distinct known loads, a, b and c are determined, which are the terms for the error box. Since the impedance, admittance, and reflection coefficient are bilinear transforms of each other, error-box parameters can be solved for any of these measurement targets.

To use the outlined calibration method, two pairs of measurement ratios ($M_{\pm N}$) are needed, which translate to five power detectors. This calibration procedure does not require any nonlinear solvers. However, obtaining an initial solution with this method and using a nonlinear solver to solve for eigenvalues can provide accuracy benefits. In the experiments and sensitivity simulations, closed form solution is deter-

mined to be sufficiently accurate. To maximize the information each load contributes, calibration loads should be selected as far apart on the Smith chart and complex loads should be preferred when possible.

4.6 Measurement Port Considerations

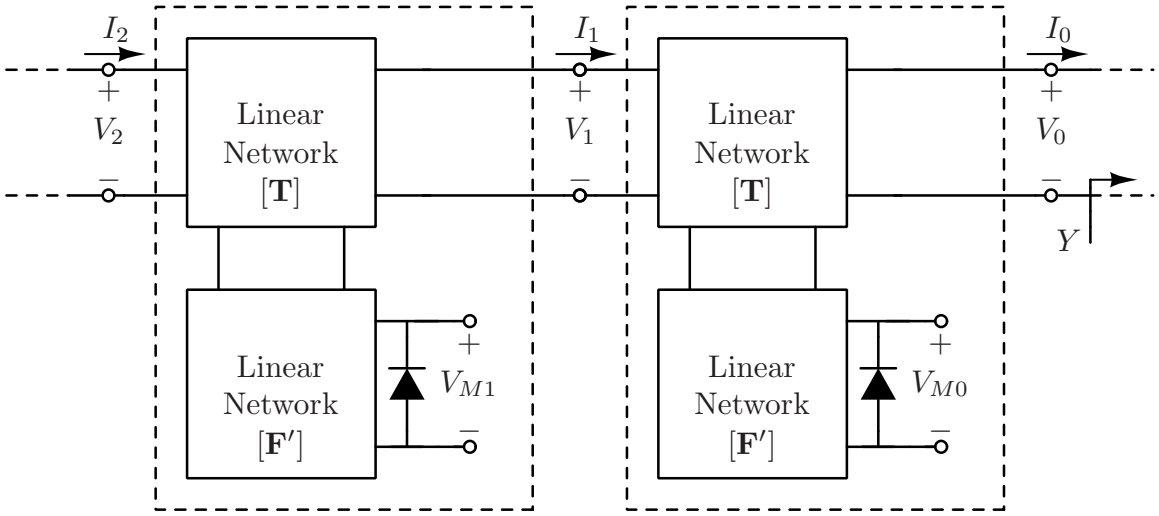

Figure 4.6: Measurements with Arbitrary Transfer Matrix

So far it has been assumed that voltages can be directly measured on the edges of unit-cells. This may not be practical in some applications. In this section, it is demonstrated that power detectors can be placed anywhere in the unit cell, and the outlined method would still work without any modifications.

First, consider the case shown in Fig. 4.6. One node in the circuit is exposed as a measurement port and the linear network that is connected to the measurement port can be arbitrarily complex. The following relation can still be expressed between the measured voltage (V_{M0}), the input voltage (V_0) and the current (I_0) to unit cell:

$$V_{M0} = AV_0 + BI_0 \tag{4.43}$$

where A, and B are arbitrary network parameters. Since V_0 is the reference port, where the admittance measurement plane is, the current can be expressed as $I_0 =$

YV_0. Then, V_{M0} becomes:

$$V_{M0} = V_0(A + BY). \tag{4.44}$$

This relation can be expressed in matrix form as the following:

$$\begin{bmatrix} V_{M0} \\ V_0 Y \end{bmatrix} = \begin{bmatrix} A & B \\ 0 & 1 \end{bmatrix} \begin{bmatrix} V_0 \\ V_0 Y \end{bmatrix}. \tag{4.45}$$

Let $\mathbf{F'}$ denote this transformation matrix

$$\mathbf{F'} = \begin{bmatrix} A & B \\ 0 & 1 \end{bmatrix}. \tag{4.46}$$

This matrix is invertible, given $A \neq 0$. Using $\mathbf{F'^{-1}}$ and $\mathbf{T}$, the voltage and the current at the next port is found, then $\mathbf{F'}$ is applied again to find measured voltage at the next port as

$$\begin{bmatrix} V_{M1} \\ I_1 \end{bmatrix} = \mathbf{F'TF'^{-1}} \begin{bmatrix} V_{M0} \\ V_0 Y \end{bmatrix} \tag{4.47}$$

both sides are divided by the reference voltage, V_{M0},

$$\begin{bmatrix} V_{M1}/V_{M0} \\ I_1/V_{M0} \end{bmatrix} = \mathbf{F'TF'^{-1}} \begin{bmatrix} 1 \\ V_0/V_{M0} Y \end{bmatrix} \tag{4.48}$$

and by using (4.44), V_0 is written in terms of V_{M0}:

$$\begin{bmatrix} V_{M1}/V_{M0} \\ I_1/V_{M0} \end{bmatrix} = \mathbf{F'TF'^{-1}} \begin{bmatrix} 1 \\ Y/(A + BY) \end{bmatrix}. \tag{4.49}$$

Let $Y_M = Y/(A + BY)$, then for any arbitrary measurement port the following can be written:

$$\begin{bmatrix} V_{MN}/V_{M0} \\ I_N/V_{M0} \end{bmatrix} = \mathbf{F'T}^N\mathbf{F'^{-1}} \begin{bmatrix} V_{M0} \\ Y_M \end{bmatrix}. \tag{4.50}$$

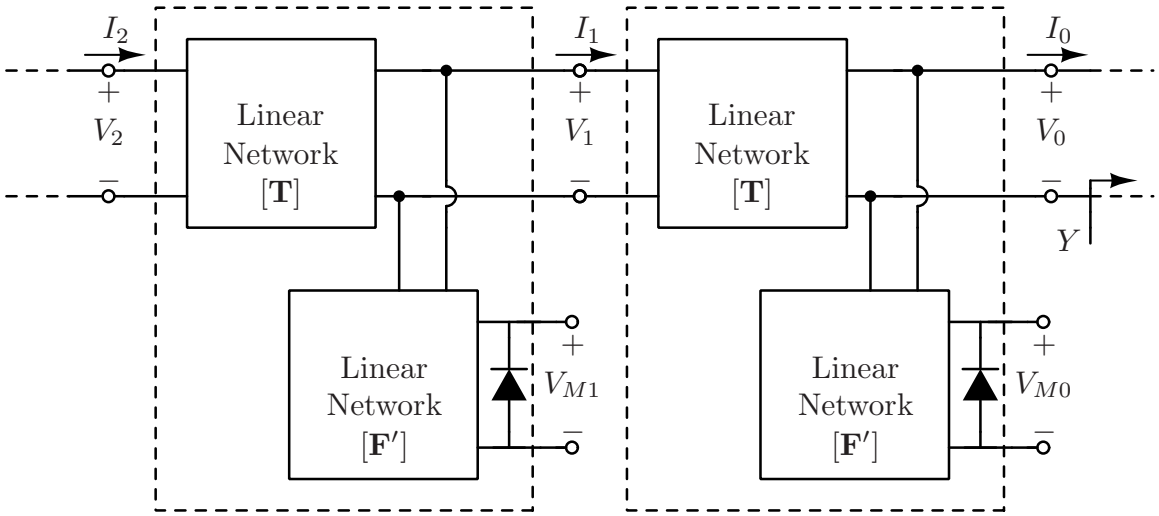

Figure 4.7: Measurements with Detectors Placed on Unit-Cell Edge

Observe that $\mathbf{F'T}^N\mathbf{F'^{-1}} = (\mathbf{F'TF'^{-1}})^N$, thus $\mathbf{T'} = \mathbf{F'TF'^{-1}}$ can be used as the unit cell transmission matrix and all previously developed methods can be applied without any modification. Also observe that eigenvalues of $\mathbf{T'}$ and $\mathbf{T}$ are equal. The measured quantity w, will be a bilinear transformation of Y_M, which can solved by using error-box calibration as described previously.

A special case of measurement port placement occurs when measurement ports are placed on the edges of the repeating unit cells (Fig. 4.7). In this configuration, Y_M would be the scaled version of Y. Also, if measurement ports are placed on the edge, one less repeating cell can be used than the arbitrary configuration. Due to these advantages, measurements ports are placed on the edge in the design example.

4.7 Dynamic Range

One of the main design goals is to select the dynamic range of the multi-port so that power at each port can be accurately measured and quantified. If the dynamic range requirement is too high, detectors may not be able to measure power accurately. Similarly, if the dynamic range is too low, quantifying measurements becomes

a challenge.

The dynamic range requirement for the power detectors is determined by multi-port parameters and the maximum VSWR or $|\Gamma|_{max}$ that should be measured. Therefore, to determine the dynamic range requirements, M_N is expressed in terms of Γ and multi-port parameters as the following:

$$M_N = \left| J_N \frac{a\Gamma + b}{c\Gamma + 1} + \frac{1}{2} L_N \right|^2 \tag{4.51}$$

where a, b, c are error-box terms that relate Γ to w. These parameters are functions of the eigenvectors, measurement port parameters and the measurement plane. M_N can be rearranged as the following to obtain the canonical six-port formula:

$$M_N = K_N \left| \frac{\Gamma + q_N}{c\Gamma + 1} \right|^2 \tag{4.52}$$

where K_N and q_N are defined as the following:

$$K_N = |(J_N a + 0.5 L_N c)|^2 \tag{4.53}$$

$$q_N = (J_N b + 0.5 L_N)/(J_N a + 0.5 L_N c). \tag{4.54}$$

Each port has an unique q_N. Let $|q|_{max}$, $|q|_{min}$ be the maximum and the minimum magnitude of q_N respectively. Also note that if $|c| \approx 0$, then q_N would correspond to the circle centers of the six-ports [37].

It is assumed that the test signal power can be adjusted to accommodate the operating region (linear region) of the power detectors. Therefore, the dynamic range (DR) of the power detectors needs to be greater or equal to the ratio of the largest (P_{max}) and the smallest value (P_{min}) that power detectors can obtain in a single measurement, which can be expressed as:

$$DR = \frac{P_{max}}{P_{min}} = \frac{M_{max}}{M_{min}} \tag{4.55}$$

where M_{max}, M_{min} are the maximum and minimum values that M_N can have for any N (including zero) in a single measurement. M_{max} and M_{min} can be found by maximizing and minimizing the nominator and denominator of (4.52) appropriately by using the triangle inequality. This approach gives the upper bound for dynamic range as the following:

$$DR = \left(\frac{|q|_{max} + |\Gamma|_{max}}{|q|_{min} - |\Gamma|_{max}} \cdot \frac{1 + |c||\Gamma|_{max}}{1 - |c||\Gamma|_{max}} \right)^2 . \tag{4.56}$$

To have a bounded dynamic range, $|q|_{min}$ and $1/|c|$ should be bigger than $|\Gamma|_{max}$. The dynamic range of a particular port can be decreased by increasing $|q|_{min}$ or decreasing $|c|$, $|q|_{max}$. Therefore, the dynamic range can be adjusted by strategically selecting eigenvalues, eigenvectors, power detector placement and the measurement plane. In a more traditional multi-port/six-port $|c| \approx 0$ achieved generally by using directional couplers, a similar result can be obtained by placing the power detector inside the unit cell. Unfortunately, placing power detectors on the edge of the unit-cell would result in $|c| > 0$, increasing the required dynamic range. Another way to decrease the required dynamic range is achieved by increasing the number of detectors. It is unlikely each detector would reach its extreme values at the same time and only one pair of $M_{\pm N}$ needs to be measured accurately to find Γ.

4.8 Monte-Carlo Simulation and Sensitivity Analysis

The main consideration of the practicality of the proposed approach are mismatches between different unit cells and power detectors. Due to process variations, each unit cell will have slightly different $\mathbf{T}$, $\mathbf{F}'$, and power detector gain. Therefore, the proposed method needs to be evaluated against such non-idealities to determine its robustness and to determine how tight tolerances should be in an application. To achieve this goal, Monte-Carlo simulations are conducted with different $\mathbf{T}$, $\mathbf{F}'$, and

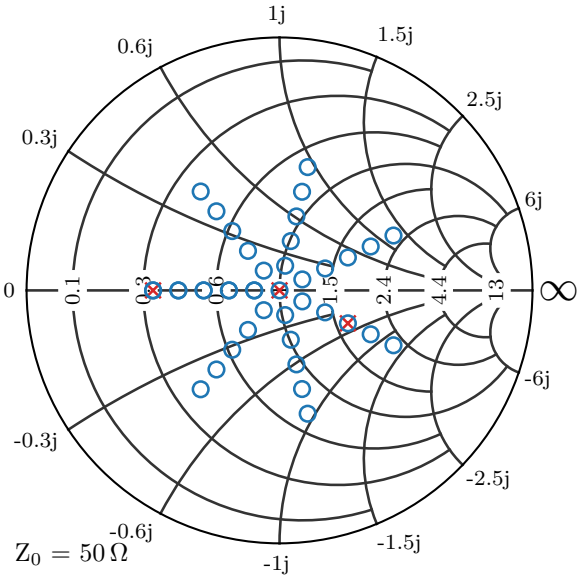

Figure 4.8: Sensitivity Test Loads, Calibration Loads are shown with (×)

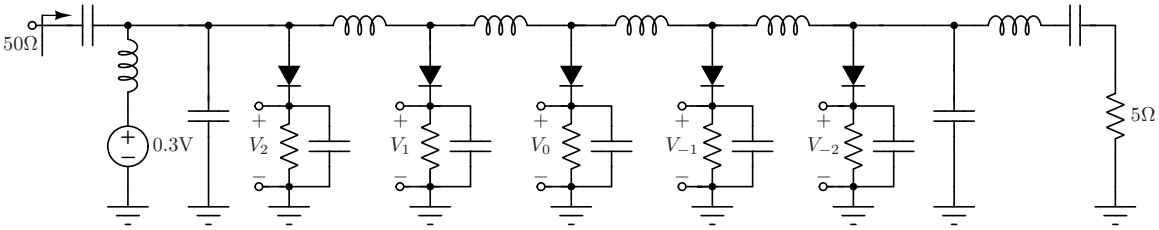

Figure 4.9: Matching Network with Power Detectors

power detector gain are used. In the simulations, power detector voltages, V_N, will be measured as:

$$\begin{bmatrix} V_N \\ I_N \end{bmatrix} = \mathbf{F}'\mathbf{T}^{N-1} \begin{bmatrix} 1 \\ Y \end{bmatrix} \tag{4.57}$$

for $N = 1 \ldots 5$, and Y will be selected as uniformly distributed loads across the Smith Chart as shown in Fig. 4.8. The VSWR for the test loads is under 3:1 ($S_{11} < -3$ dB), to simulate a realistic application. For each load, 1000 random mismatches are generated. M_N defined as:

$$M_N = \left| \frac{V_N}{V_3} \right|. \tag{4.58}$$

First, two matrices $\mathbf{T}$ for the unit cell, and $\mathbf{F}'$ for the measurement port are

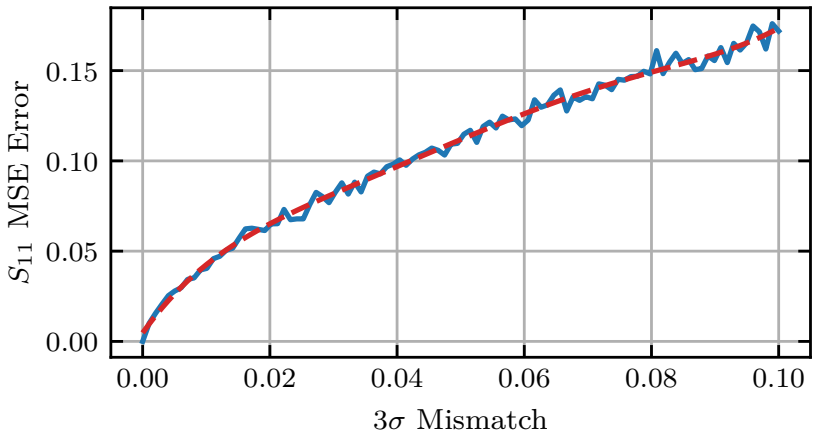

(a) MSE between Loads and Measurements in S_{11} Domain

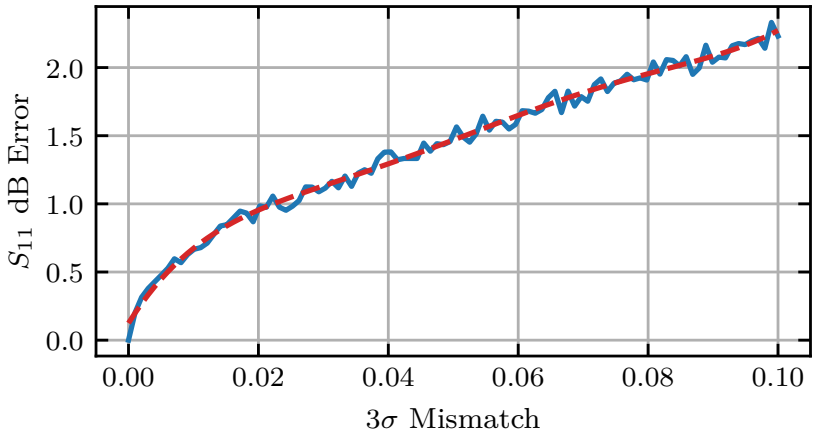

(b) dB Error between Loads and Measurement in S_{11} Domain

Figure 4.10: Monte-Carlo Simulation, (—) Calculated, (- -) Polynomial Trend

constructed. The real and imaginary part of the entries of $\mathbf{T}$ (t_{ij}) and $\mathbf{F}'$ (f_{ij}) will be randomly sampled from the uniform distribution $U[-1, 1]$.

After verifying that the randomly constructed matrices have an inverse, $\mathbf{T}$ will be normalized such that $\det \mathbf{T} = 1$. This ensures that $\mathbf{T}$ represents a physical reciprocal circuit, which is an underlying assumption for the proposed theory. Now that the matrix for the unit cell and the measurement port are constructed, random mismatches can be added for each unit cell to introduce non-idealities. For each unit cell, two mismatch matrices will be constructed, one for the $\mathbf{T}$ and another one for the $\mathbf{F}'$.

These mismatch matrices will be term-wise multiplied with the unit cell matrices. $\mathbf{T}$, $\mathbf{F}'$ with mismatches added is denoted as $\mathbf{T}_N$, $\mathbf{F}'_N$ and their entries are denoted as t_{Nij}, f_{Nij} respectively. These entries can be expressed as

$$t_{Nij} = t_{ij} \cdot m^t_{Nij} \tag{4.59}$$

$$f_{Nij} = f_{ij} \cdot m^f_{Nij} \tag{4.60}$$

where, m^t_{Nij}, m^f_{Nij} are added mismatches to respective entries. These mismatches will be sampled from the normal distribution with a mean (μ) one.

$$m^t_{Nij} \sim \mathcal{N}(1, \sigma_t^2) \tag{4.61}$$

$$m^f_{Nij} \sim \mathcal{N}(1, \sigma_f^2). \tag{4.62}$$

The last non-ideality that will be simulated is gain mismatch between power detectors. To model this, measured voltage is multiplied with a randomly sampled gain $g_N \sim \mathcal{N}(1, \sigma_g^2)$. The mean of the gain is selected as one since voltages are normalized. Therefore, the measured voltage at each port can be expressed as:

$$V_N = \begin{bmatrix} g_N & 0 \end{bmatrix} \mathbf{F}'_N \prod_{i=1}^{N-1} \mathbf{T}_i. \tag{4.63}$$

In order to determine the tolerance, the 3σ of all mismatch distributions is swept from 0 to 0.1. This would mean that 99.9% of units have less than the specified mismatch. For example, if $3\sigma = 0.1$ this would mean 99.9% of mismatches are below 10%. All mismatches ($\mathbf{T}$, $\mathbf{F}'$, gain) will be simulated together to determine maximum tolerable mismatch.

The randomly created systems will measure S_{11} of the predetermined set of loads that are shown in Fig. 4.8. The system is calibrated using the three known S_{11} values by using the method described in the previous section.

Simulation results showed that (Fig. 4.10) to keep measurement error under 1 dB, all combined mismatches should be below 2%. This is easily achievable by discrete

parts, and it is expected to be easily achievable in an integrated application since most RF components are much bigger than the smallest node feature size.

It is also determined that the proposed technique has highest sensitivity to measurement port errors ($\mathbf{F}'$), followed by gain mismatches. The proposed technique is least sensitive to the mismatches between unit cells ($\mathbf{T}$).

4.9 Design Example

For hardware demonstration, one embodiment of the proposed technique is designed. In this design, a periodic-structure multi-port is embedded into a two-section LC matching network that transforms $5\,\Omega$ to $50\,\Omega$. The $5\,\Omega$ represents the impedance seen by a hypothetical PA, and $50\,\Omega$ represents the impedance of a hypothetical antenna. In the simulation and in the experiment, developed method is used to detect changes in the $50\,\Omega$ port.

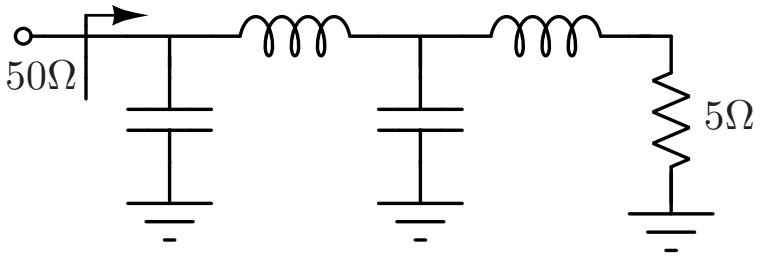

Figure 4.11: Two Section LC Matching Network

The two-section LC matching network without any modifications is shown in Fig. 4.11. A multi-port based on the proposed measurement method is embedded into this network by dividing the inductor on the left into four smaller inductors (Fig. 4.9). Simple peak detectors are connected to the edges of the divided inductors to measure the voltage incident upon the nodes. The peak detector diodes (BAT15-02LRH) are biased such that they are barely open during operation. To achieve this, high value resistors ($100\,\mathrm{k}\Omega$) are connected in series to diodes, so when a diode turns on, the

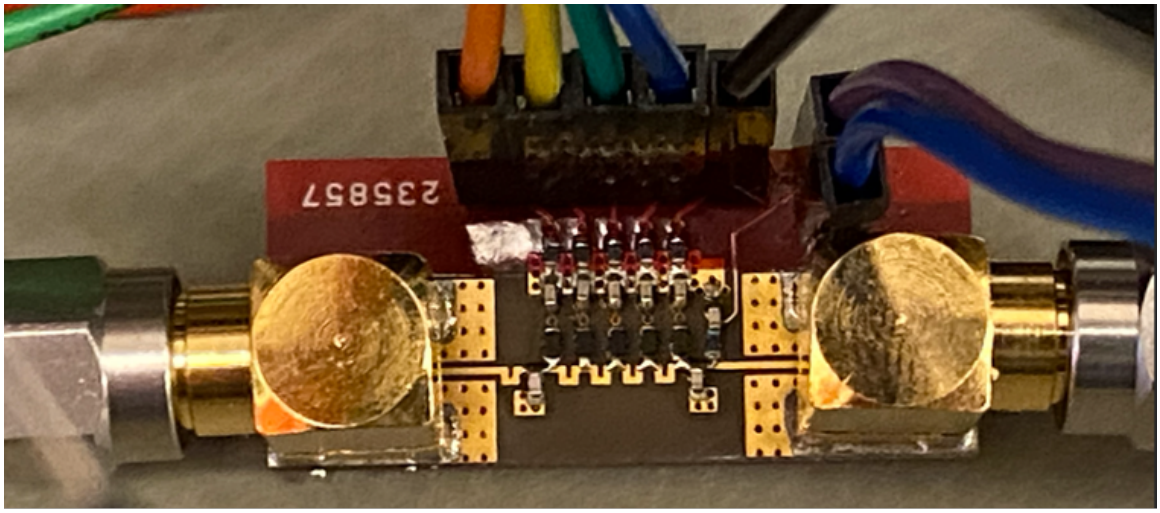

(a) Matching Network with Power Detectors

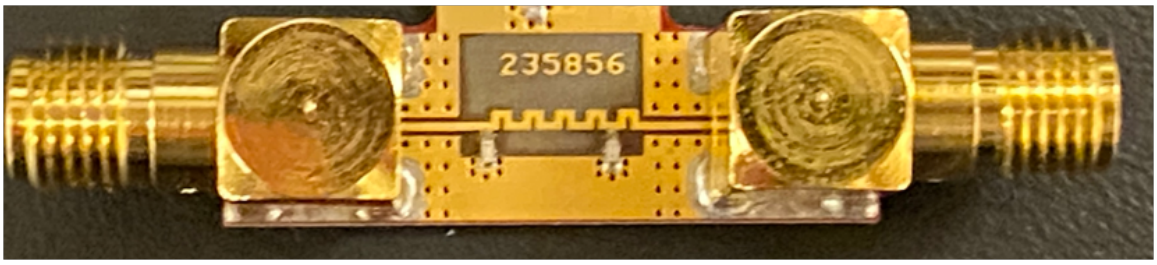

(b) Matching Network without Power Detectors

Figure 4.12: Fabricated Boards

current through them will be minimal. Finally, a shunt capacitance is connected to the ground, so high frequency signals have a low resistance return path. This design enables the peak detectors to measure low voltages without impacting the matching network performance significantly.

The matching network needs to be co-designed with the power detectors due to the small added capacitance. The proposed circuit schematic (with DC blocks) is shown in Fig. 4.9, and the fabricated board is shown in Fig. 4.12(a). As can be seen in Fig. 4.12(a) in the physical design of the matching network, both LC sections have a microstrip inductor and a lumped capacitor. Microstrip inductors are used due to

their high-Q and the ease of matching between different unit cells.

Normally, an ideal series component would not have a diagonalizable transmission matrix. However, due to the parasitic capacitance of the inductors each unit cell consists of a mix of shunt and series components. This is also verified with the co-simulation of the design.

The co-simulation consists of two parts: EM simulation of the PCB layout, and the lumped models of the discrete devices provided by the manufacturers. The main assumption in the proposed theory is that there are repeating structures in the circuit that can be leveraged to extract more information. In the EM simulation, this assumption can be violated by how meshes are constructed. This can affect the measurement procedure negatively, but it can be resolved by simulating a single unit cell and measurement port. Then, unit cells, measurement ports, discrete components and the rest of the layout are connected in the circuit simulation. This guarantees that each unit cell and measurement port have the same response.

The design is simulated with 193 loads regularly distributed across the Smith

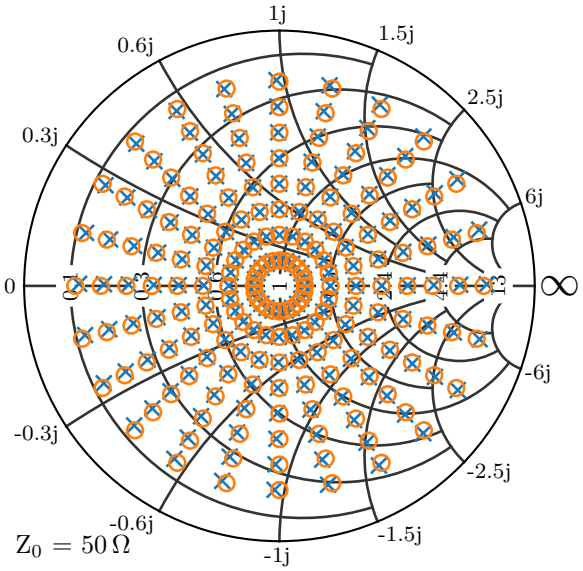

Figure 4.13: Design Simulation Results - Test Loads (○), Measured Values (×)

Chart used as test loads. Test loads have VSWR under 10:1 ($S_{11} < -2$ dB). Fig. 4.13 shows the test load locations and the measurement results for each load. It is clear from Fig. 4.13 that the proposed method measures S_{11} with high accuracy. Simulations show that 10:1 VSWR requires 19 dB and 3:1 VSWR requires 12 dB of dynamic range from the power detectors. This dynamic range requirement is expected to be lower in the real hardware experiment due to additional losses resulting from the experiment.

4.10 Hardware Experiment

To show the feasibility of the proposed method, two hardware experiments are conducted. In the first experiment, it is verified that the proposed method does not degrade matching network performance. In the second experiment, it is verified that the proposed method can measure loads with high accuracy.

4.10.1 Impact on Hardware Performance

One board with (Fig. 4.12(a)) and another board without power detectors (Fig. 4.12(b)) are fabricated. Then, two boards are compared to see whether the proposed technique degrades the performance of the matching network. TRL calibration is used to deembed the SMA connectors from the VNA measurements. In TRL calibration, impedances are normalized to the characteristic impedance of the transmission line (Z_0). Therefore, to measure the real values of the loads, Z_0 of the transmission line needs to be known. A high precision 50 Ω load is included with the TRL calibration kit. Using this included known impedance, Z_0 is found to be 46 Ω, which also agrees with the EM simulation. When the matching network is co-designed with the proposed method, adding the power detectors does not degrade insertion loss (Fig. 4.15(a)) and impedance matching performance (Fig. 4.15(b)) of the matching

network. These results also agree with the EM simulation. Overall, both boards transform 50Ω to 5Ω with central frequency of 2.5GHz. The reflection coefficients characteristic agrees with the EM simulation and the two minimums observed verifies that the two section matching works as expected.

4.10.2 Measurement Accuracy

An adjustable load across a wide range of frequencies is measured with a VNA (Agilent E8361A). As shown in Fig. 4.16, the adjustable load is constructed with a diode (BAT15-02LRH) and a fixed resistor. When the diode is completely off ($V_{ctrl} = 0$), it will act as a high impedance load looking into the RF input (V_{RF}). As the control voltage is increased (V_{ctrl}), the diode will become a short circuit and the fixed resistance (50 Ω) will dominate the input impedance. There will be a rotation around the Smith Chart due to the transmission line between the adjustable load and the rest of the system. This rotation will also change with frequency. When these two effects are combined, a wide range of loads will be created and sweep across the Smith Chart. V_{ctrl}, will control how far away the load is from the center of the Smith Chart, and frequency will control the angle of the load.

A signal generator is connected to the board. The frequency sweep and sweep run outputs of the signal generator are connected to a microcontroller (Arduino) board. These outputs will facilitate the frequency synchronization between the signal generator and measurements. The control voltage for the adjustable load is generated by a DAC (MCP4725). The outputs of the peak detectors are connected to ADC (ADS1115). The entire process is coordinated by the microcontroller connected to a computer over USB. The experiment diagram and a picture of the setup are shown in Fig. 4.14.

Power detectors are characterized with a power sweep from −30 dBm to 17 dBm

with 1 dB steps. Power sweep values and corresponding DC output from a power detector are plotted against each other in Fig. 4.18. A line is fitted in this graph to determine the DC offset and the dynamic range of the power detectors. The lower and upper limits of the detector outputs are determined using this model. The output voltage is within 2% of the linear trend from 0.28 V to 1.58 V, corresponding to a 15 dB dynamic range.

By using adjustable load and frequency sweep, 1407 test data points (excluding calibration data points) are obtained. The performance of the proposed method is evaluated across frequency, different reflection coefficients and phases. The design center frequency is 2.5 GHz, and the method can reliably work from 1.5 GHz to 3.5 GHz (Fig. 4.17), which corresponds to 80% fractional bandwidth. This means, the proposed method can easily work with high bandwidth antennas. The test loads require at most 13.5 dB of dynamic range in a single measurement, which is consistent with the simulation results.

Fig. 4.17 shows the system performance across frequency. Fig. 4.20 shows the comparison between test loads and measured values in the Smith Chart. Not all data points are included in these two figures to enable readability. The included data points are selected at random and to cover of a wide range of the Smith Chart. Fig. 4.19 shows the magnitude and phase of the measured S_{11} with respect to the baseline (measured by the VNA) for all loads. Fig. 4.17-4.19, do not include any calibration loads since they have zero measurement errors by definition.

These results show that, proposed design and method can measure a wide variety of reflection coefficients with high accuracy. Another observation is the max. dB error increases when low magnitudes are measured. This is expected because, as the magnitude drops, even very small measurement errors in magnitude would result in significant errors in dB domain. The highest dB error is 1.6 dB for loads that have

$S_{11} > -10\,\text{dB}$. Overall, the system can measure S_{11} phase very reliably. The error summary is given in Table-4.1.

The biggest constraint that limits the accuracy of the system is the linearity of the power detectors. It has been observed that, accuracy can be changed significantly if input power is above or below certain values. Therefore, input power should be carefully selected so that power detectors are working in the linear region.

Table 4.1: Error Summary Table

	All Loads	
	S_{11} ***Mag. Error (dB)***	S_{11} ***Phase Error (°)***
Max	2.5 dB	7.9°
Avg*	0.23 dB	0.53°
	Loads $S_{11} > -10\,\text{dB}$	
	S_{11} ***Mag. Error (dB)***	S_{11} ***Phase Error (°)***
Max	1.57 dB	4.3°
Avg*	0.26 dB	0.5°

* Calibration loads are not included.

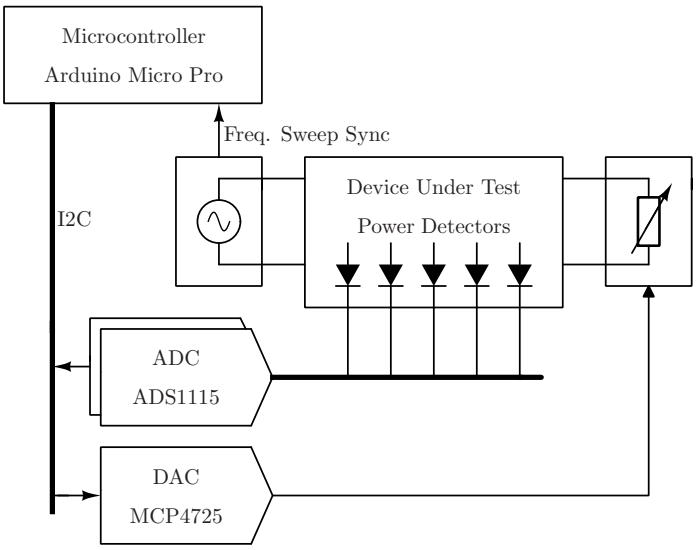

(a) Experiment Block Diagram

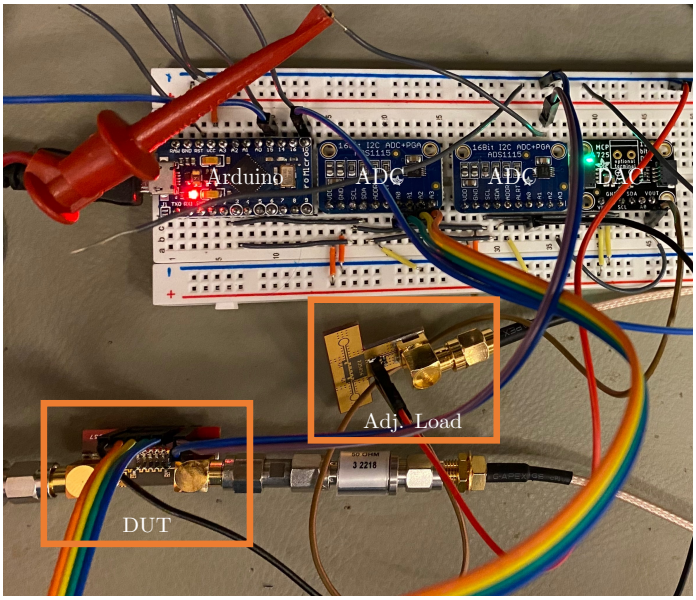

(b) Experiment Setup

Figure 4.14: Hardware Experiment

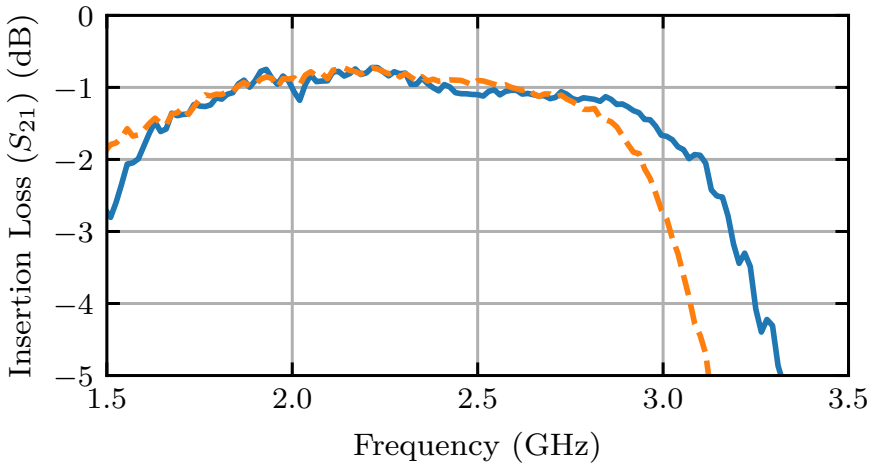

(a) Insertion Loss

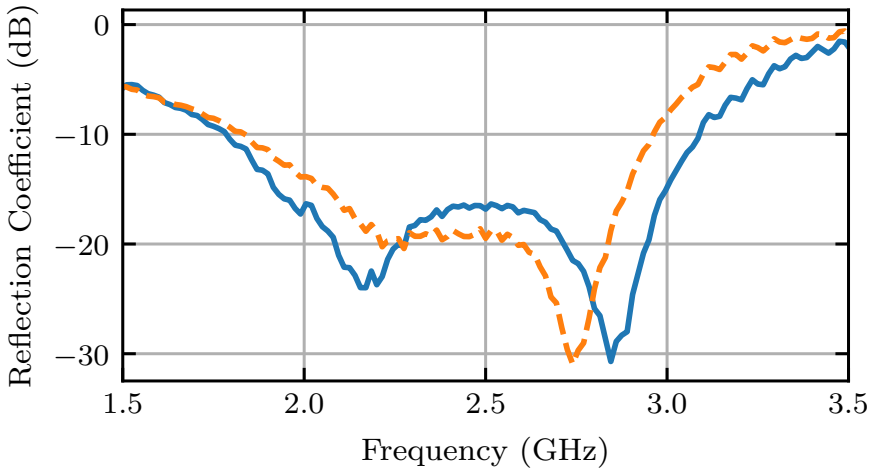

(b) Reflection Coefficient

Figure 4.15: Matching Network Performance with (—) and without (- -) Power Detectors

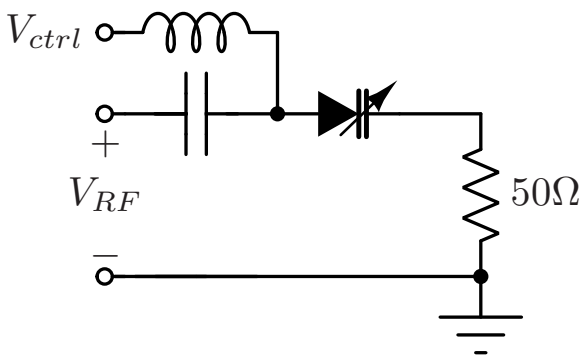

Figure 4.16: Adjustable Load Schematic

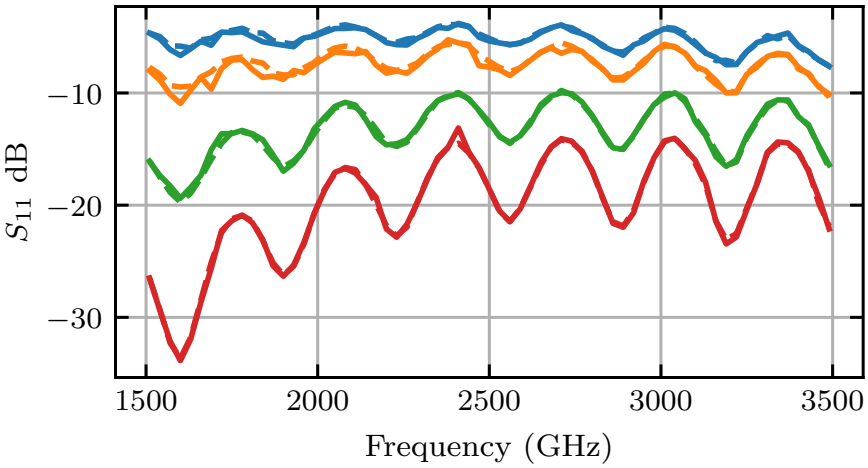

(a) S_{11} dB

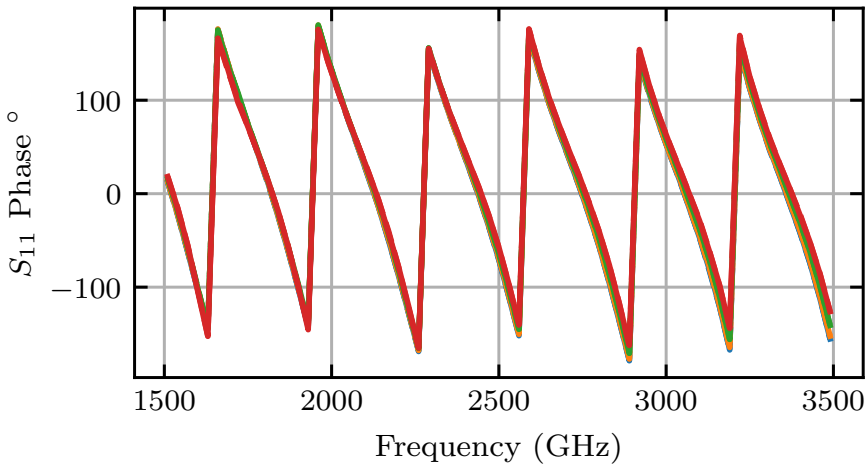

(b) Phase of S_{11} in degrees

Figure 4.17: S_{11} of various test loads (Dashed) vs Measured (Solid) vs Frequency

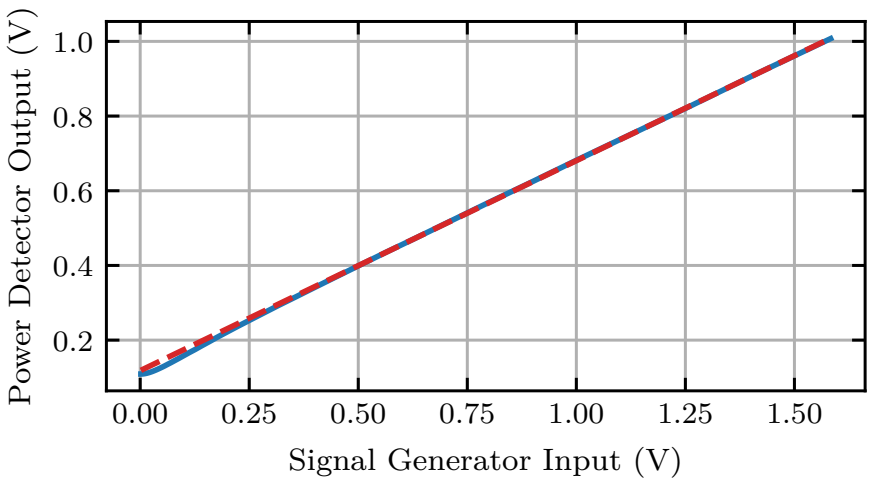

Figure 4.18: Power Detector Output Voltage (—), Fitted Line (- -)

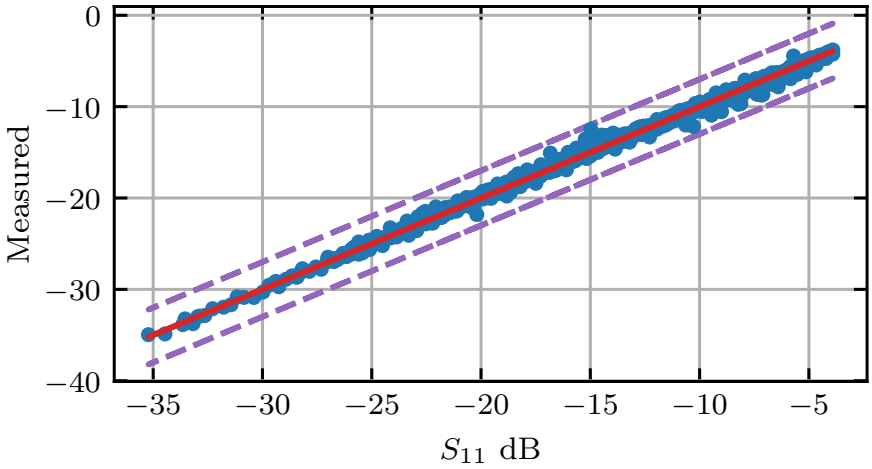

(a) S_{11} dB, 3 dB error line (- -)

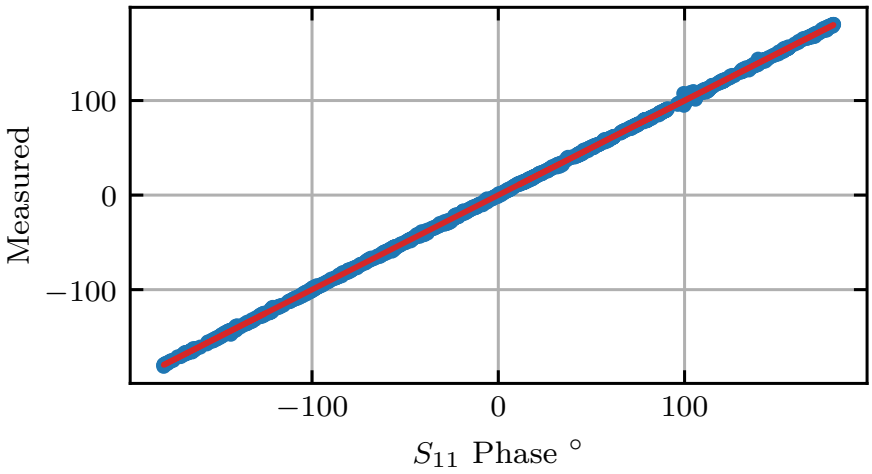

(b) Phase of S_{11} in degree

Figure 4.19: S_{11} of All Test Loads (—) vs Measurement (•)

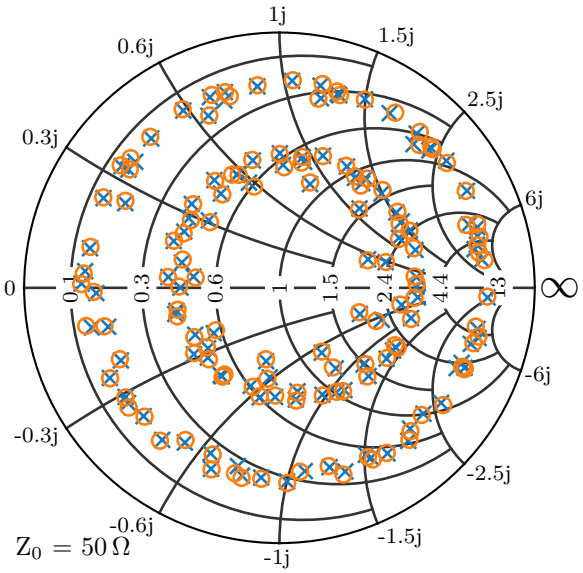

Figure 4.20: Design Experiment Results - Test Loads (○), Measured Values (×)

Chapter 5

IMPEDANCE COMPARISON AND CONJUGATE MATCHING MEASUREMENT USING PERIODIC STRUCTURES AS SIX-PORTS

In this chapter, we proposed a method for quantifying conjugate matching between two loads by using periodic structures and injecting a test signal in different points of the periodic structure. The proposed method does not disrupt the operation of the system while taking measurements, and the proposed signal injecting scheme does not require a series connected switch in the signal path. Additionally, the proposed method does not require any external calibration, and can measure the ratio of two loads or the mismatch between two loads. The proposed method is verified in both simulation and hardware experiments. The hardware experiment results show that the proposed method provides good accuracy and high bandwidth for measuring mismatch between two loads. The proposed method can be used in scenarios where conjugate matching between two loads is important for the operation of the system.

5.1 Comparing Loads with Symmetric Unit-Cells

Symmetric unit cell is defined as a cell with a transmission matrix that has the same diagonal entries, which can be expressed as:

$$\mathbf{T} = \begin{bmatrix} A & B \\ C & A \end{bmatrix}. \tag{5.1}$$

If an unit cell is symmetric, then its eigenvalues (v_1, v_2) are opposite signs of each other ($v_1 = -v_2$), therefore $k = -1$. This simplifies w:

$$w = \frac{Yv}{2} \tag{5.2}$$

This means, w is simply a scaled version of the admittance. If admittance, or impedance wants to be measured directly, this scaling factor is extracted, but if we would like to just measure the ratio (r) of two loads, this extraction is not necessary as demonstrated in Fig. 5.1. The ratio between two loads in Fig. 5.1 is given as:

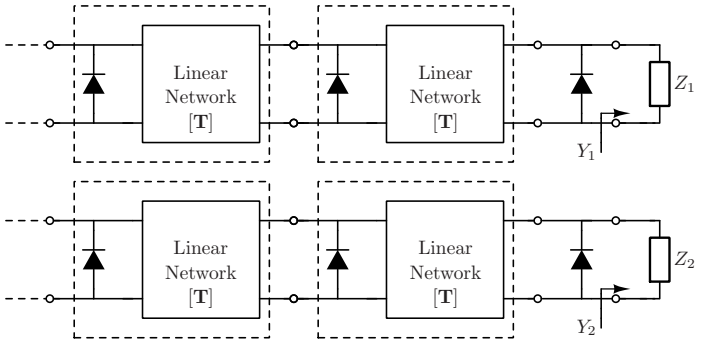

Figure 5.1: Comparing Admittances Using Matched Measurement Systems

$$r = \frac{w_1}{w_2} = \frac{Y_1}{Y_2} = \frac{Z_2}{Z_1} \tag{5.3}$$

In some applications, quantifying conjugate matching between two loads using the reflection coefficient as a mismatch metric is desired. In this cases reflection coefficient (Γ) is given by:

$$\Gamma = \frac{Z_L - Z_S^*}{Z_L + Z_S^*} \tag{5.4}$$

where Z_L is load impedance and Z_S is source impedance. If these terms are replaced with corresponding $Z_S = v/w_S$, $Z_L = v/w_L$:

$$\Gamma = \frac{1/w_L - 1/w_S^*}{1/w_L + 1/w_S^*} = \frac{Z_L/v - Z_S^*/v^*}{Z_L/v + Z_S^*/v^*} \tag{5.5}$$

v and v^* should be equal to cancel each other to make (5.5) same as (5.4). Meaning $v = v^*$, therefore v should be a real number.

So far, we assumed that power measurements are taken at the edge of the periodic structures but this is not necessary. Power detectors can be placed anywhere inside

the unit-cell and all the developed theory will work without any modifications [39]. Placing power detectors on the edge of the unit-cells is advantageous. This placement reduces the required unit-cells and the measured Y is the scaled version of the actual load admittance, unlike the arbitrary power detector placement, which only guarantees measured Y to be the bilinear transform of the actual load [39]. Therefore, in the proposed method, power detectors are placed on the edges of the unit cells as shown in Fig. 5.2.

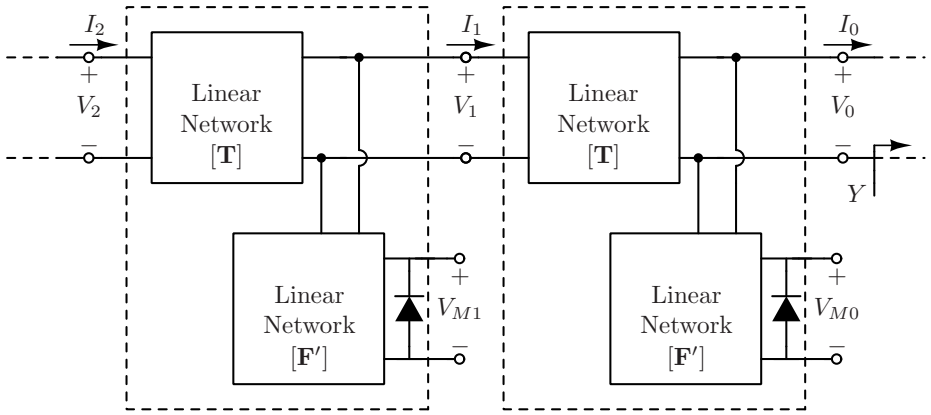

Figure 5.2: Edge Connected Power Detectors

5.2 Method for Measuring Conjugate Matching

The proposed method uses test signal injection on both sides of the periodic structure to measure two loads without disrupting the system operation. The exact placement of the test signal injection point is not important, and it can be different in different nodes. Only critical part is signals should be injected different sides, and should not be injected on any part of the periodic structure. Fig.5.3(a) shows the the proposed measurement system. The proposed measurement system consists of two test signal paths which can have different output impedances and power detectors connected to the unit cells. The number of power detectors can be selected based on the application requirements such as dynamic range, sensitivity, bandwidth and

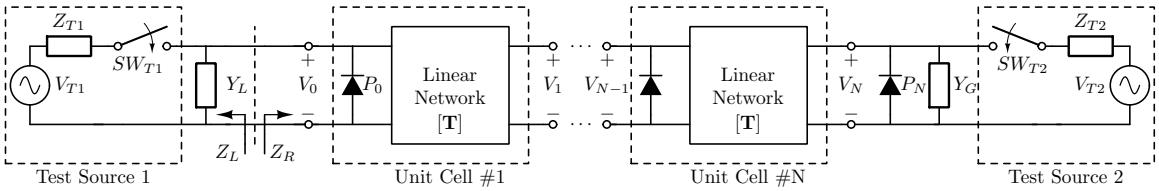

(a) Proposed BIST Structure

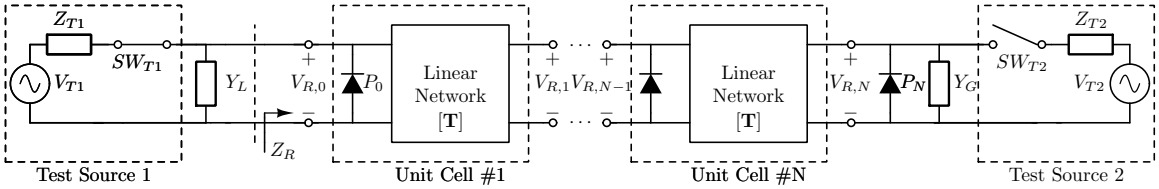

(b) BIST Configuration for Measuring Z_R

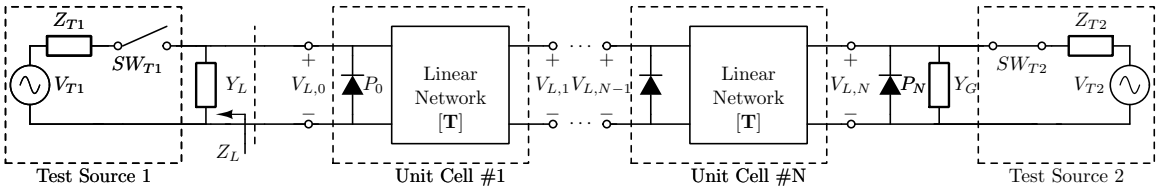

(c) BIST Configuration for Measuring Z_L

Figure 5.3: BIST Structure and Configurations for Measuring Z_R and Z_L Relative to Each Other

accuracy.

The test signal sources can be disconnected from the system in the mission mode or when monitoring is deemed unnecessary. The mission mode operation is demonstrated in Fig.5.3(a). The test signal sources are connected sequentially in two steps in the monitoring/test mode. In each step, a test signal is injected from one side of the periodic structure and power measurements are recorded. The test mode operation is demonstrated in Fig.5.3(c)-(b).

One point that needs attention is when the test signal injection changes directions, so does the numbering of the power detectors. The power detector number N decreases from source to load. Therefore, the sign of N changes when the direction of

the test signal changes. This is equivalent to taking the conjugate of the measured w. This should be taken into account when w_L and w_R are calculated. If the numbering scheme of the power detectors are not changed between the measurement steps, the conjugate of one of the parameters is readily calculated. After the power measurements are recorded using two distinct loads, the difference between the normalized measurements should be calculated. If the total difference between normalized measurements are lower than a certain threshold, two loads are almost conjugates of each other. If the sum of the difference is larger than the threshold, then we need to calculate λ to calculate w_L and w_R.

An initial solution for λ should be selected based on simulation or other prior knowledge. w_L and w_R should be calculated using corresponding power measurement values P_{-1}, P_0 and P_1. Then, the corresponding fourth power measurement P_2 for w_L and w_R should be calculated using λ, w_L, w_R and by plugging these values in 4.16. The difference between the calculated value for P_2 is based on the mathematical model and the measured value of P_2 should be minimized using the gradient based nonlinear solvers. We found that the trust region reflective method algorithm is suitable for this problem. These recorded measurements are then used for calculating w_L and w_R as described in the previous section. If v is a real number, w_L and w_R values can be plugged back into (5.4) to quantify the conjugate mismatch between two loads. A flowchart for measuring conjugate matching using the proposed method is given in Fig. 5.4.

5.3 Design Example

To accurately measure the conjugate matching, we need a symmetric unit cell with a transmission matrix that has real eigenvectors. The transmission matrix of a transmission line with length l, propagation constant γ and characteristic impedance

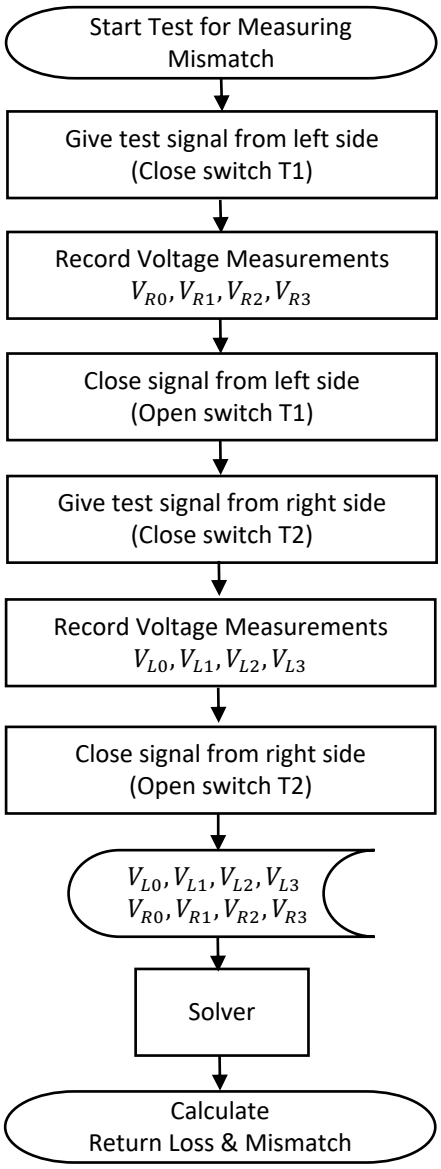

Figure 5.4: Conjugate Matching Measurement Flowchart

Z_0 is given as:

$$\mathbf{T} = \begin{bmatrix} \cosh(\gamma l) & Z_0 \sinh(\gamma l) \\ \sinh(\gamma l)/Z_0 & \cosh(\gamma l) \end{bmatrix} \tag{5.6}$$

The eigenvalues of this matrix is $v = \pm Z_0$ and the eigenvectors are $\lambda = e^{\pm\gamma l}$. For low-loss lines Z_0 is can be approximated as a real number, and propagation constant can be approximated as $\gamma \approx j2\pi/\lambda$, where λ is the wavelength of the RF signal.

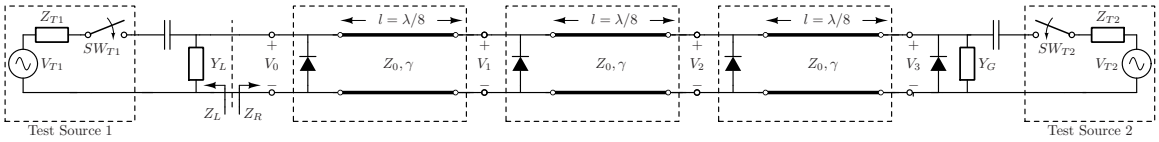

Figure 5.5: BIST Design Example

Therefore, a low-loss transmission line meets all the requirements for the proposed method. A power detector (LTC5532) is connected to each node through a capacitor, to measure the power at each node.

We need to maximize our measurement sensitivity respect to directly measured parameters. If we plug in the values for the transmission line into (4.21):

$$B_1 = \mathrm{Re}\left\{J_1 L_1^* w\right\} = \mathrm{Re}\left\{(e^{\gamma l} - e^{-\gamma l})(e^{\gamma l} + e^{-\gamma l})w\right\} \tag{5.7}$$

$$= \mathrm{Re}\left\{4j\sin(\gamma l)\cos(\gamma l)w\right\} \tag{5.8}$$

$$= -2sin(2\gamma l)\,\mathrm{Im}\left\{w\right\} \tag{5.9}$$

To find the sensitivity our measurement to load changes, we can take derivative respect to $\mathrm{Im}\{w\}$:

$$\frac{\partial B_1}{\partial\,\mathrm{Im}\,w} = 2\sin(2\gamma l) = 2\sin\left(\frac{4\pi}{\lambda}l\right) \tag{5.10}$$

which is maximized when $l = \lambda/8$. After B_1 is measured, it is used with $|J_1 L_1 w|^2$ measurement to find the imaginary part of the w. If we follow the same steps as described before, we will find that $l = \lambda/8$ also maximizes the sensitivity of this magnitude measurement. Therefore, the unit-cell of the proposed periodic structure will consist of a $\lambda/8$ transmission line and a power detector as shown in Fig. 5.6 to maximize the measurement sensitivity. This sensitivity calculations also shows, the system will work best when we operate near the design frequency. As we away from the design frequency, sensitivity of the system will reduce and inevitably give inaccurate measurement results.

The loading of the power detector would slightly change the eigenvector of the unit-cell, but in simulation we found the impact of this is insignificant to the measurement performance. The overall measurement system design is given in Fig. 5.5.

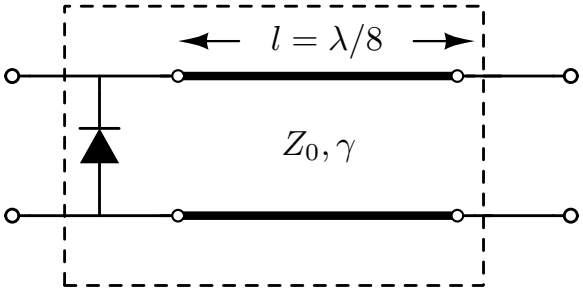

Figure 5.6: Proposed Unit Cell

5.4 Simulation Results

The proposed design is first verified with simulation. In the simulation, individual transmission line segments and coupling capacitors are simulated in the EM simulation. Then, extracted EM models and impedance information of the power detectors are used in the circuit simulation to create design given in Fig. 5.5. In the circuit simulation, one load is held constant while the other load is swept across the Smith Chart. The voltage readings from the power detector ports are recorded, and processed as described in the previous section. The mismatch between the swept load and the fix load is extracted and compared with the measured mismatch by the proposed method. As shown in Fig. 5.7, the measured mismatch and the simulated mismatch are in agreement, confirming the validity of the proposed method and the design.

5.5 Hardware Experiment

To verify the practicality of the method, hardware experiments are done with the fabricated board (Fig. 5.8) based on the design example shown in Fig. 5.5. Two

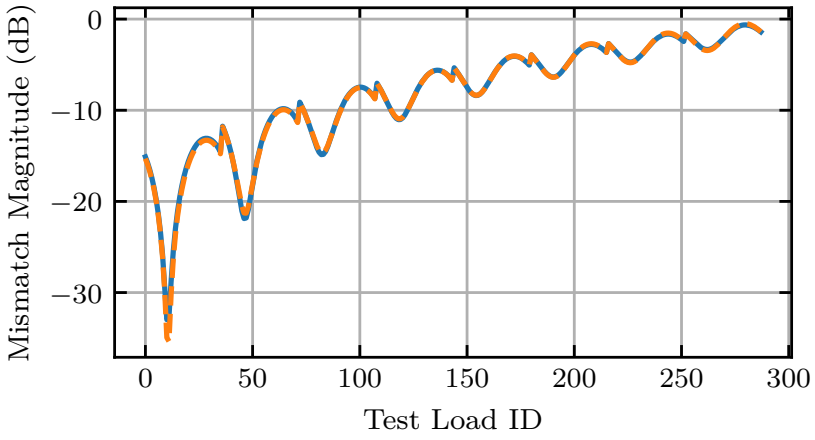

(a) Mismatch Magnitude Measurement

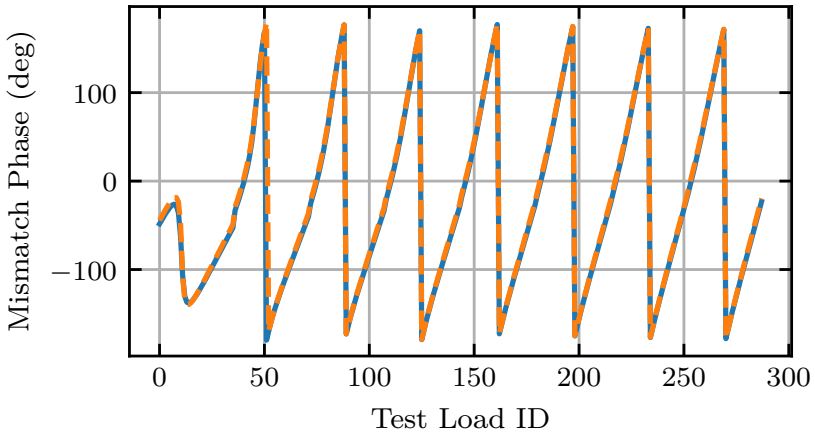

(b) Mismatch Phase Measurement

Figure 5.7: Mismatch Meas. Simulation - Measured (—) vs Simulated (- -)

switch boards are connected in two ends of the test board to facilitate the signal switching. To show the capabilities of the proposed method under a wide range of load conditions, an adjustable load is constructed with a phase shifter (HMC647A) and an open ended lossy transmission line. The phase shifter presents slightly different losses for each phase shift, and the phase shift effect also rotates the load around the Smith Chart. These two effects create a wide range of loads around the Smith Chart. The created loads are measured by a VNA (Agilent E8361A) to provide baseline measurements. The adjustable load is connected to the one end of the test board and

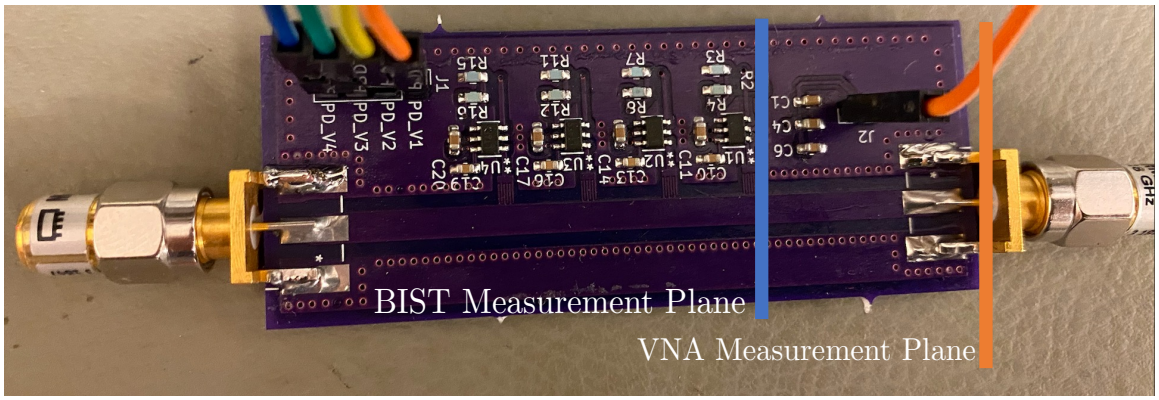

Figure 5.8: Fabricated Board

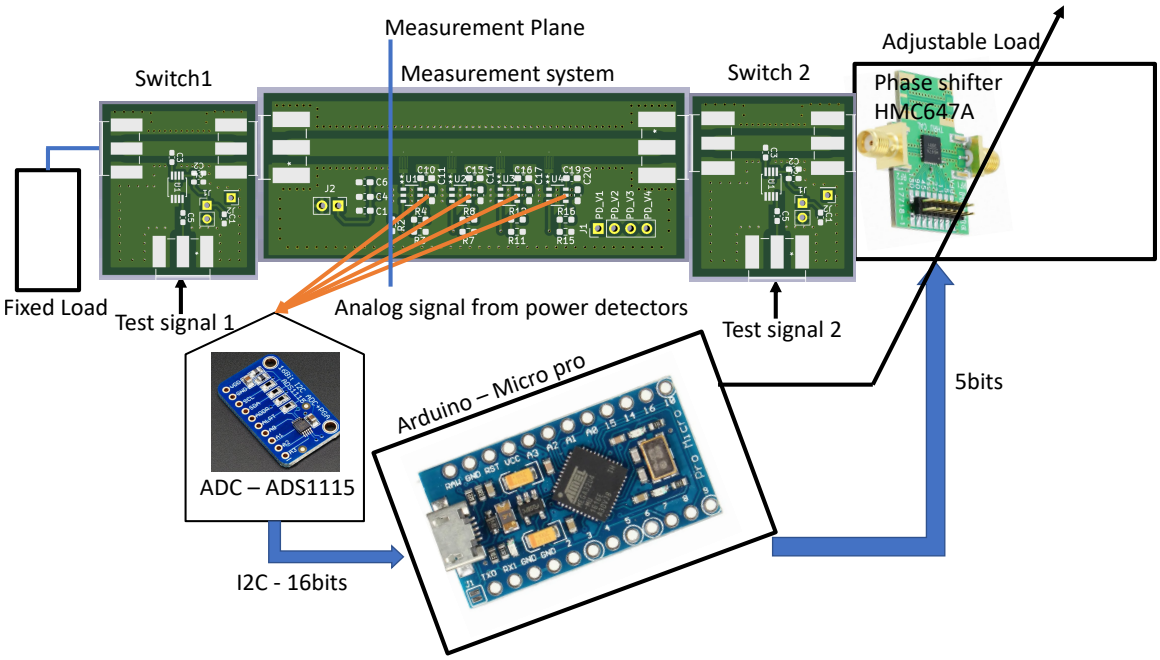

Figure 5.9: Experiment Diagram

the other end of the test board is terminated with a 50 Ω load. Before connecting the adjustable load, another set of measurements are taken looking into the board by the VNA, establishing a conjugate matching measurement plane demonstrated in Fig. 5.8. Using these load measurements, conjugate matching is calculated with respect to the VNA measurement plane.

The experiment diagram is shown in Fig. 5.9 and the hardware experiment setup is shown in Fig. 5.10. The experiment is conducted by following the flowchart shown

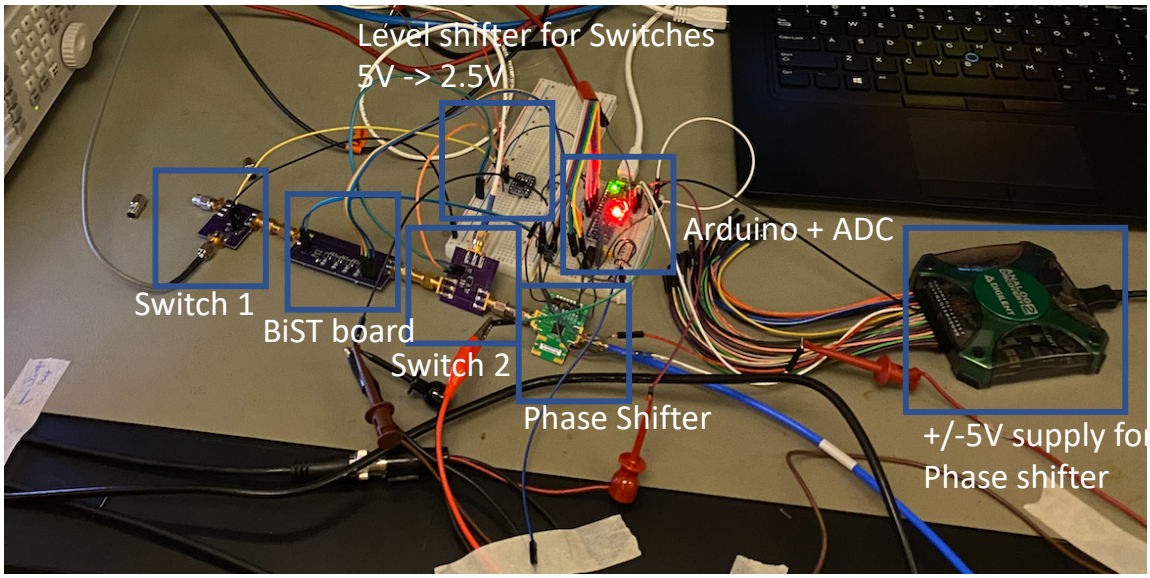

Figure 5.10: Experiment Setup

in Fig. 5.4. The test signals are generated by two signal generators and power detector outputs are measured by an ADC (ADS1115). The entire process is coordinated by a microcontroller connected to a PC.

Due to the difference between the VNA and BIST measurement planes shown in Fig. 5.8, there is an almost constant difference in the magnitude and phase of the VNA and BIST measurements. These disagreements disappear when the BIST measurement plane is moved to same VNA measurement plane by using the three term error model. The three term error model is a bilinear transform that models the effect of the network between the VNA and BIST planes. This model is extracted by mapping three BIST measurements to three corresponding VNA measurements. After the deembedding, BIST and VNA measurements are in agreement, verifying the difference was due to measurement plane locations. As shown in Fig.5.11-5.12, the proposed method can measure the mismatch reliably and the proposed design example based on this method has a wide bandwidth. The design example can reliably quantify the conjugate matching from 2.2 GHz to 3 GHz corresponding to 30%

fractional bandwidth.

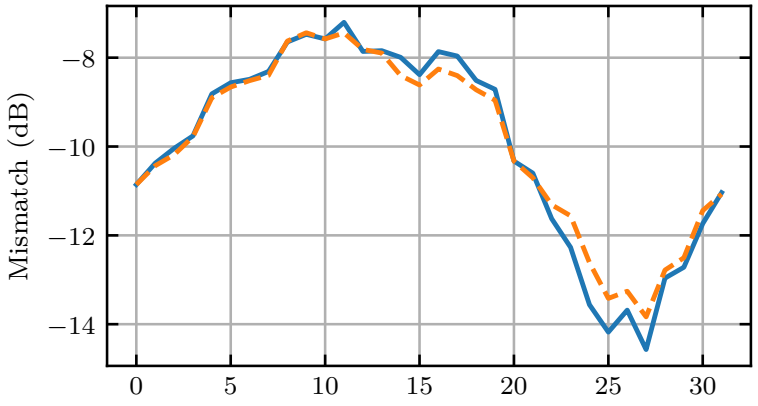

(a) Mismatch Mag. Meas. @ 2.2 GHz

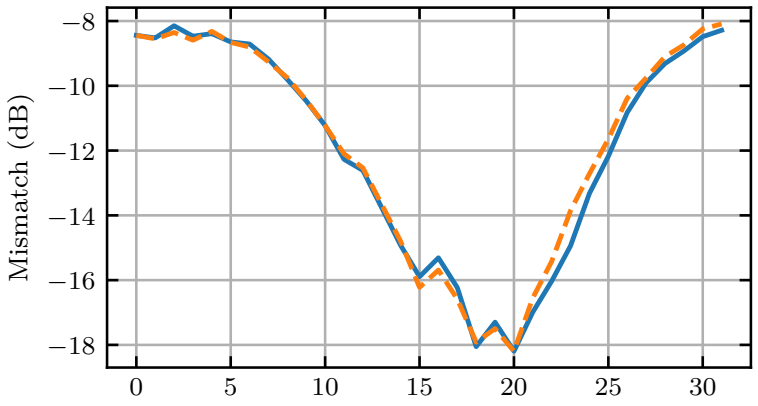

(b) Mismatch Mag. Meas. @ 2.6 GHz

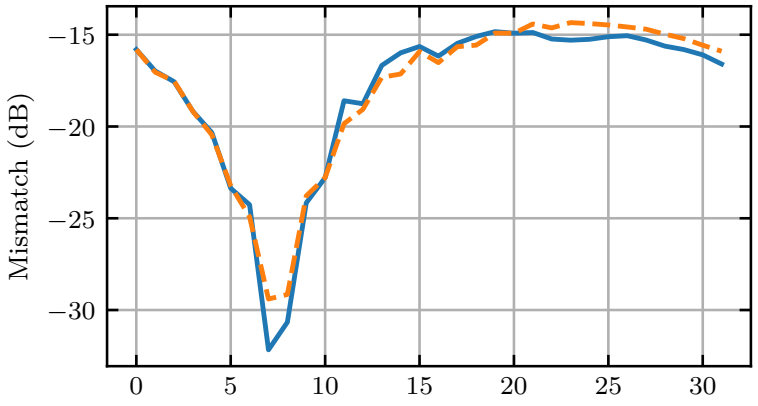

(c) Mismatch Mag. Meas. @ 3 GHz

Figure 5.11: Mismatch Mag. Measurements Proposed Method (—) vs VNA (- -) Measurement Plane Deembedded

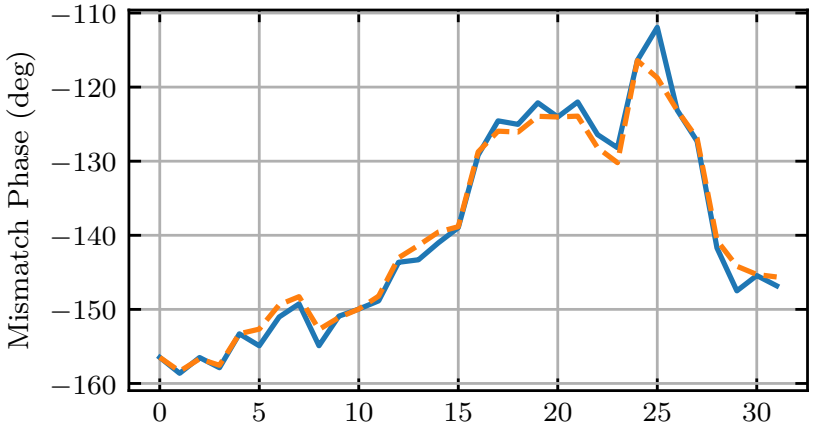

(a) Mismatch Phase Meas. @ 2.2 GHz

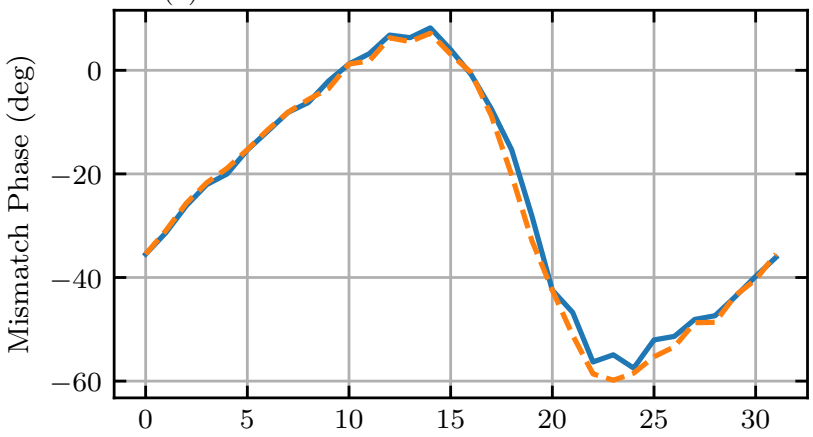

(b) Mismatch Phase Meas. @ 2.6 GHz

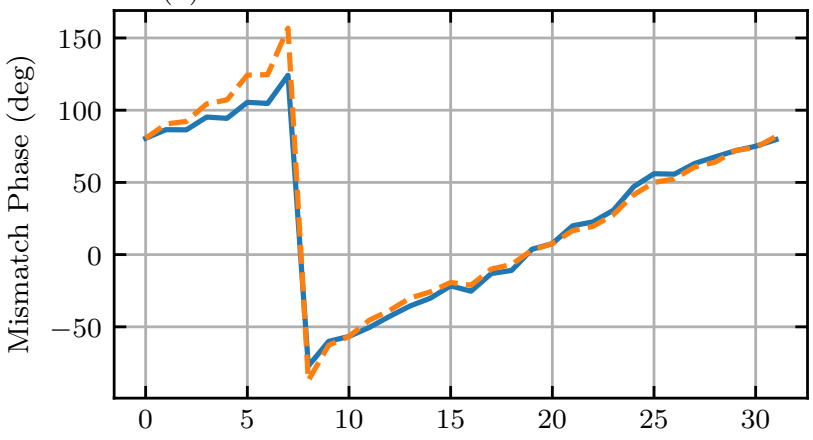

(c) Mismatch Phase Meas. @ 3 GHz

Figure 5.12: Mismatch Phase Measurements Proposed Method (—) vs VNA (- -) Measurement Plane Deembedded

Chapter 6

CONCLUSION

In this thesis, we explored different design approaches and techniques for multi-port network analyzers. First, we gave a detailed analysis for minimizing the impact of the noise on the measurement. We verified analysis using simulation. This analysis resulted in unique multi-port parameters and different cost functions that have different advantages. These new parameters are verified using hardware experiments.

Another limiting factor in applications is required computing resources for calibration and measurement. To overcome these challenges, we proposed using periodic structures as multi-ports. When we apply periodic-structure constraint on multi-ports, the theory simplifies significantly and enables us to come up with closed form calibration and measurement procedures for multi-ports. Additionally, periodic structures guarantee that if power measurements are correctly done, there would be always a unique solution for power detector measurements. This finding simplifies design procedure significantly, and open doors for richer family of multi-port designs. Periodic structures as multi-port is verified with simulations and hardware experiments. In the hardware experiment, we embedded periodic multi-port directly into a matching network. The embodiment of the method gave good accuracy across different VSWR measurements.

Each application has different needs, and not every application requires absolute measurement of the impedance value. For such applications, we proposed using periodic multi-ports to compare two loads. Periodic multi-port theory enabled us to come up with a technique that enables us to compare two loads without requiring calibration or known design parameters. The proposed technique verified with simulation

and hardware experiments. In the hardware experiment, we placed power detectors in regular intervals on a transmission line and measured conjugate mismatch between two loads using novel signal injection technique. We verified the proposed technique can quantify conjugate matching between two loads with high accuracy.

REFERENCES

[1] D. Gomez, M. Sroka, and J. L. G. G. Jimenez, "Process and temperature compensation for rf low-noise amplifiers and mixers," *IEEE Transactions on Circuits and Systems I: Regular Papers*, vol. 57, no. 6, pp. 1204–1211, 2009.

[2] H. K. Subramaniyan, E. A. Klumperink, V. Srinivasan, A. Kiaei, and B. Nauta, "Rf transconductor linearization robust to process, voltage and temperature variations," *IEEE journal of solid-state circuits*, vol. 50, no. 11, pp. 2591–2602, 2015.

[3] K. Choi and D. J. Allstot, "Parasitic-aware design and optimization of a cmos rf power amplifier," *IEEE Trans. on Circuits and Systems I: Regular Papers*, vol. 53, no. 1, pp. 16–25, 2006.

[4] M. Javid and J. Kitchen, "A multilevel pulse-width modulated class-e power amplifier," in *2019 IEEE Radio and Wireless Symposium (RWS)*. IEEE, 2019, pp. 1–4.

[5] M. Youssef, A. Zolfaghari, H. Darabi, and A. Abidi, "A low-power wideband polar transmitter for 3g applications," in *2011 IEEE International Solid-State Circuits Conference*. IEEE, 2011, pp. 378–380.

[6] Y. Wang, R. Wu, J. Pang, D. You, A. A. Fadila, R. Saengchan, X. Fu, D. Matsumoto, T. Nakamura, R. Kubozoe *et al.*, "A 39ghz 64-element phased-array cmos transceiver with built-in calibration for large-array 5g nr," in *2019 IEEE Radio Frequency Integrated Circuits Symposium (RFIC)*. IEEE, 2019, pp. 279–282.

[7] D. Chang, S. Ozev, O. Sinanoglu, and R. Karri, "Approximating the age of rf/analog circuits through re-characterization and statistical estimation," in *2014 Design, Automation & Test in Europe Conference & Exhibition (DATE)*. IEEE, 2014, pp. 1–4.

[8] D. Chang, S. Ozev, B. Bakkaloglu, S. Kiaei, E. Afacan, and G. Dundar, "Reliability enhancement using in-field monitoring and recovery for rf circuits," in *2014 IEEE 32nd VLSI Test Symposium (VTS)*. IEEE, 2014, pp. 1–6.

[9] D. Chang, J. N. Kitchen, S. Kiaei, and S. Ozev, "In-field recovery of rf circuits from wearout based performance degradation," *IEEE Transactions on Emerging Topics in Computing*, vol. 8, no. 2, pp. 442–452, 2017.

[10] J. Joh and J. A. del Alamo, "Rf power degradation of gan high electron mobility transistors," in *2010 International Electron Devices Meeting*. IEEE, 2010, pp. 20–2.

[11] A. Chini, V. Di Lecce, M. Esposto, G. Meneghesso, and E. Zanoni, "Rf degradation of gan hemts and its correlation with dc stress and i-dlts measurements," in *2009 European Microwave Integrated Circuits Conference (EuMIC)*. IEEE, 2009, pp. 132–135.

[12] E. S. Erdogan and S. Ozev, "Detailed characterization of transceiver parameters through loop-back-based bist," *IEEE Transactions on Very Large Scale Integration (VLSI) Systems*, vol. 18, no. 6, pp. 901–911, 2009.

[13] R. B. Staszewski, I. Bashir, and O. Eliezer, "Rf built-in self test of a wireless transmitter," *IEEE Transactions on Circuits and Systems II: Express Briefs*, vol. 54, no. 2, pp. 186–190, 2007.

[14] J. W. Jeong, J. Kitchen, and S. Ozev, "Robust amplitude measurement for rf bist applications," in *2015 20th IEEE Europ. Test Symposium (ETS)*, 2015, pp. 1–6.

[15] J. W. Jeong, A. Nassery, J. N. Kitchen, and S. Ozev, "Built-in self-test and digital calibration of zero-if rf transceivers," *IEEE Transactions on Very Large Scale Integration (VLSI) Systems*, vol. 24, no. 6, pp. 2286–2298, 2016.

[16] A. Nassery and S. Ozev, "An analytical technique for characterization of transceiver iq imbalances in the loop-back mode," in *2012 Design, Automation Test in Europe Conference Exhibition (DATE)*, 2012, pp. 1084–1089.

[17] J. W. Jeong, J. Kitchen, and S. Ozev, "A self-compensating built-in self-test solution for rf phased array mismatch," in *2015 IEEE International Test Conference (ITC)*, 2015, pp. 1–9.

[18] M. E. Avci and S. Ozev, "Background receiver iq imbalance correction for in-field and post-production testing and calibration," in *2021 IEEE International Test Conference (ITC)*, 2021.

[19] M. Shafiee, N. Beohar, P. Bakliwal, S. Roy, D. Mandal, B. Bakkaloglu, and S. Ozev, "A disturbance-free built-in self-test and diagnosis technique for dc-dc converters," *ACM Transactions on Design Automation of Electronic Systems (TODAES)*, vol. 23, no. 2, pp. 1–22, 2017.

[20] M. Ince, E. Yilmaz, W. Fu, J. Park, K. Nagaraj, L. Winemberg, and S. Ozev, "Fault-based built-in self-test and evaluation of phase locked loops," *ACM Transactions on Design Automation of Electronic Systems (TODAES)*, vol. 26, no. 3, pp. 1–18, 2021.

[21] C. A. Balanis, *Antenna theory: analysis and design*. John wiley & sons, 2016.

[22] J. W. Jeong, J. Kitchen, and S. Ozev, "A self-compensating built-in self-test solution for rf phased array mismatch," in *2015 IEEE International Test Conference (ITC)*. IEEE, 2015, pp. 1–9.

[23] D. M. Pozar, *Microwave engineering*. John wiley & sons, 2011.

[24] E. Zenteno, M. Isaksson, and P. Händel, "Output impedance mismatch effects on the linearity performance of digitally predistorted power amplifiers," *IEEE Trans. Microw. Theory Techn.*, vol. 63, no. 2, pp. 754–765, 2015.

[25] F. Balteanu, "Rf front end module architectures for 5g," in *2019 IEEE BiCMOS and Compound Semicon. Intgr. Circ. and Tech. Symp. (BCICTS)*, Nov. 2019, pp. 1–8.

[26] K. Boyle, E. Spits, M. De Jongh, S. Sato, T. Bakker, and A. van Bezooijen, "Gain statistics for mobile phone antenna tuners," in *2013 7th European Conf. on Ant. and Prop. (EuCAP)*, Apr. 2013, pp. 432–436.

[27] G. D. Singh, H. M. Nemati, and L. C. N. de Vreede, "A low-loss load correction technique for self-healing power amplifiers using a modified two-tap six-port network," *IEEE Trans. Microw. Theory Techn.*, vol. 69, no. 9, pp. 4069–4081, July 2021.

[28] V. Solomko, W. Bakalski, A. Cattaneo, D. Tayari, P. Nascimento, J. Essel, and A. Thomas, "Rf impedance sensor for antenna-tuning front ends," *IEEE Trans. Microw. Theory Techn.*, vol. 68, no. 3, pp. 1095–1102, Dec. 2019.

[29] K. Staszek, "Balanced six-port reflectometer with nonmatched power detectors," *IEEE Trans. Microw. Theory Techn.*, vol. 69, no. 11, pp. 4869–4878, Aug. 2021.

[30] J. A. Qayyum, A. A. Nawaz, M. Ko, A. Malignaggi, D. Kissinger, and A. C. Ulusoy, "A 94-ghz five-port reflectometer for measuring complex reflection coefficient using 0.13-μm sige hbt detectors," in *2018 IEEE Topi. Conf. on Wireless Sens. and Sens. Netw. (WiSNet)*, Jan. 2018, pp. 77–79.

[31] F. Wiedmann, B. Huyart, E. Bergeault, and L. Jallet, "New structure for a six-port reflectometer in monolithic microwave integrated-circuit technology," *IEEE Trans. on Instr. and Meas.*, vol. 46, no. 2, pp. 527–530, Apr. 1997.

[32] T. Lasri, N. Rolland, D. Glay, B. Gorisse, H. El Aabbaoui, and K. Haddadi, "A fully inp monolithic integrated millimeter-wave reflectometer," in *2006 Europ. Microw. Conf*, Sep. 2006, pp. 703–706.

[33] A. Grebennikov, G. Haider, and J.-p. Forstner, "Rf circuit with improved antenna matching," U.S. Patent 8 471 756, Jun. 25, 2013.

[34] H. Song, B. Bakkaloglu, and J. T. Aberle, "A cmos adaptive antenna-impedance-tuning ic operating in the 850mhz-to-2ghz band," in *2009 IEEE Intern. Solid-State Circ. Conf.*, Feb. 2009, pp. 384–385.

[35] D. Ji, J. Jeon, and J. Kim, "A novel load mismatch detection and correction technique for 3g/4g load insensitive power amplifier application," *IEEE Trans. Microw. Theory Techn.*, vol. 63, no. 5, pp. 1530–1543, Apr. 2015.

[36] S. A. Paul, M. Goldenberg, and A. Eshraghi, "Adaptively tuned rf power amplifier," U.S. Patent 7 911 277, Mar. 22, 2011.

[37] G. F. Engen, "The six-port reflectometer: An alternative network analyzer," *IEEE Trans. Microw. Theory Techn.*, vol. 25, no. 12, pp. 1075–1080, Dec. 1977.

[38] B. Hur and W. R. Eisenstadt, "Automated wideband test system, measurement uncertainty, and design of on-chip six-port reflectometers for 5g applications," in *2015 85th Microw. Meas. Conf. (ARFTG)*, May 2015, pp. 1–5.

[39] M. E. Avci and S. Ozev, "Low-overhead rf impedance measurement using periodic structures," *IEEE Transactions on Microwave Theory and Techniques*, 2023.

[40] ——, "Design optimization for n-port rf network reflectometers under noise and gain imperfections," in *2020 IEEE Intern. Test Conf. (ITC)*, Nov. 2020, pp. 1–10.

[41] D. T. Donahue, P. E. de Falco, and T. W. Barton, "Power amplifier with load impedance sensing incorporated into the output matching network," *IEEE Trans. on Circ. and Syst. I: Reg. Papers*, vol. 67, no. 12, pp. 5113–5124, June 2020.

[42] R. Caldecott, "The generalized multiprobe reflectometer and its application to automated transmission line measurements," *IEEE Trans. on Ant. and Prop.*, vol. 21, no. 4, pp. 550–554, July 1973.

[43] G. F. Engen, "An improved circuit for implementing the six-port technique of microwave measurements," *IEEE Trans. Microw. Theory Techn.*, vol. 25, no. 12, pp. 1080–1083, Dec. 1977.

[44] S. Yeo and M. Cheng, "Novel nine-port network analyser for measuring scattering coefficients of two-port devices," *IEE Proceedings-Microwaves, Antennas and Propagation*, vol. 143, no. 2, pp. 137–140, 1996.

[45] C. A. Hoer, "A network analyzer incorporating two six-port reflectometers," *IEEE Trans. Microw. Theory Techn.*, vol. 25, no. 12, pp. 1070–1074, 1977.

[46] L. Oldfield, J. Ide, and E. Griffin, "A multistate reflectometer," *IEEE Trans. on Instr. and Meas.*, no. 2, pp. 198–201, 1985.

[47] C. A. Hoer, "Calibrating a six-port reflectometer with. four impedance standards," National Bureau of Standards, Tech. Rep., March 1979.

[48] K. Haddadi and T. Lasri, "Formulation for complete and accurate calibration of six-port reflectometer," *IEEE Trans. Microw. Theory Techn.*, vol. 60, no. 3, pp. 574–581, Feb. 2012.

[49] J. Hunter and P. Somlo, "An explicit six-port calibration method using five standards (short papers)," *IEEE Trans. Microw. Theory Techn.*, vol. 33, no. 1, pp. 69–72, Jan. 1985.

[50] S. Li and R. G. Bosisio, "Calibration of multiport reflectometers by means of four open/short circuits," *IEEE Trans. Microw. Theory Techn.*, vol. 30, no. 7, pp. 1085–1090, July 1982.

[51] F. Ghannouchi and R. Bosisio, "An alternative explicit six-port matrix calibration formalism using five standards," *IEEE Trans. Microw. Theory Techn.*, vol. 36, no. 3, pp. 494–498, Mar. 1988.

[52] G. F. Engen, "Calibrating the six-port reflectometer by means of sliding terminations," *IEEE Trans. Microw. Theory Techn.*, vol. 26, no. 12, pp. 951–957, Dec. 1978.

[53] F. Wiedmann, B. Huyart, E. Bergeault, and L. Jallet, "A new robust method for six-port reflectometer calibration," *IEEE Trans. on Instr. and Meas.*, vol. 48, no. 5, pp. 927–931, Oct. 1999.

[54] K. Staszek, "Six-port calibration utilizing matched load and unknown calibration loads," *IEEE Trans. Microw. Theory Techn.*, vol. 66, no. 10, pp. 4617–4626, July 2018.

[55] Y. Yoon, H. Kim, H. Kim, K.-S. Lee, C.-H. Lee, and J. S. Kenney, "A 2.4-ghz cmos power amplifier with an integrated antenna impedance mismatch correction system," *IEEE Journ. of Solid-State Circ.*, vol. 49, no. 3, pp. 608–621, Jan. 2014.

[56] A. Van Bezooijen, M. A. De Jongh, F. Van Straten, R. Mahmoudi, and A. H. Van Roermund, "Adaptive impedance-matching techniques for controlling l networks," *IEEE Trans. on Circ. and Syst. I: Reg. Papers*, vol. 57, no. 2, pp. 495–505, June 2009.

[57] D. Nicolas, A. Serhan, A. Giry, T. Parra, and E. Mercier, "A fully-integrated soi cmos complex-impedance detector for matching network tuning in lte power amplifier," in *2017 IEEE Radio Freq. Int. Circ. Symp. (RFIC)*, June 2017, pp. 15–18.

[58] M. E. Avci, S. Ozev, and Y. C. Kumar, "Fast rf mismatch calibration using built-in detectors," in *2022 IEEE 40th VLSI Test Symp. (VTS)*, Apr. 2022, pp. 1–7.

[59] J. Gil and H. Shin, "A simple wide-band on-chip inductor model for silicon-based rf ics," *IEEE Trans. Microw. Theory Techn.*, vol. 51, no. 9, pp. 2023–2028, Aug. 2003.

[60] scipy.optimize.minimize. [Online]. Available: https://docs.scipy.org/doc/scipy/reference/generated/scipy.optimize.minimize.html

[61] K. Subburaj, B. Ginsburg, P. Gupta, K. Dandu, S. Samala, D. Breen, K. Ramasubramanian, T. Davis, Z. Parkar, D. Shetty *et al.*, "Monitoring architecture for a 76-81ghz radar front end," in *2018 IEEE Radio Frequency Integrated Circuits Symposium (RFIC)*. IEEE, 2018, pp. 264–267.

[62] A. Kumar, S. Samala, K. Subburaj, and C. Kumar Y.B. Awr1243 cascade application report. [Online]. Available: http://www.ti.com/lit/an/swra574a/swra574a.pdf